

1 **A global view of the stratospheric background, volcanic and**  
2 **wildfire aerosol in the CALIOP era (2006 – 2023)**

3 Bengt G. Martinsson, Johan Friberg, and Moa K. Sporre

4 Department of Physics, Lund University, Lund, Sweden

5 *Correspondence to:* Bengt G. Martinsson (bengt.martinsson@fysik.lu.se)

6 **Abstract.** This study deals with the stratospheric aerosol during the 17 years of lidar  
7 measurements with CALIOP. To obtain extinction from the backscattering  
8 measurements, we estimated the lidar ratios of the main aerosol injections into the  
9 stratosphere. The stratospheric background is estimated by making a subdivision of the  
10 stratosphere into nine parts, spanned by three latitude and altitude intervals, reaching  
11 background conditions individually at different times. The extracted background shows  
12 excellent agreement with solar occultation measurements in the volcanically quiescent  
13 period 1998 - 2000. Our results show that 70% of the background aerosol in the deep  
14 Brewer-Dobson (dBD) branch is formed above 19 km altitude, indicating strong  
15 influence of carbonyl sulfide on the stratospheric background aerosol. The stratosphere  
16 was clearly affected by 15 volcanic eruptions and 5 wildfires. Their combined aerosol  
17 load affected Southern extratropics, tropics and Northern extratropics almost equally,  
18 and the altitude distribution shows that the shallow Brewer-Dobson branch was most  
19 affected (43%) followed by the dBD (31%) and lowermost stratosphere (26%). The most  
20 important events in order of maximum AOD were the Hunga Ha’apai eruption (2022),  
21 Australian wildfires (2019-20) and the eruptions of Raikoke (2019), Sarychev (2009) and  
22 Nabro (2011). These events induced strong variability in the stratospheric aerosol  
23 optical depth (AOD), causing highly variable climate impact in the period studied with  
24 yearly average global effective radiative forcing ranging from  $-0.14 \text{ W/m}^2$  at background  
25 conditions to  $-0.4 \text{ W/m}^2$ . CALIOP provided important data for stratospheric aerosol  
26 climatologies during its 17 years of operation.

27

## 28 **1. Introduction**

29 Tropospheric air, containing aerosol particles and the sulfurous aerosol precursor gases  
30 carbonyl sulfide (OCS) and sulfur dioxide (SO<sub>2</sub>), enter the stratosphere across the  
31 tropical tropopause. These constituents form the stratospheric background aerosol  
32 (Kremser et al., 2016), an aerosol layer that is located above 20 km altitude in the  
33 tropics, and lower in the extratropics, containing water-soluble sulfur-rich particles  
34 (Junge et al., 1961). Additional aerosol, that can be classified as background due to its  
35 diffuse nature, originates from the Asian Tropopause Aerosol Layer (ATAL), an aerosol  
36 layer between 13 – 18 km altitude over Asia (Vernier et al., 2015). The stratospheric  
37 background aerosol contains sulfate, water, organics, and minor traces of tropospheric  
38 aerosol and extraterrestrial material (Martinsson et al., 2005; Murphy et al., 2007;  
39 Kremser et al., 2016; Martinsson et al., 2019).

40 The stratospheric aerosol load is highly variable due to special aerosol events  
41 connected to volcanism (Bauman et al., 2003; Vernier et al., 2009; Solomon et al., 2011;  
42 Andersson et al., 2015) and wildfires (Fromm et al., 2010; Martinsson et al., 2022;  
43 Friberg et al., 2023, Peterson et al., 2025), which inject copious amounts of aerosol and  
44 precursor gases affecting the stratospheric aerosol for months up to several years  
45 (Friberg et al., 2018). These aerosol events induce a variability that needs to be  
46 accounted for in climate models. From 1979, the satellite measurement era, the most  
47 important volcanic eruptions, El Chichon in 1982 and Mt. Pinatubo (1991), caused a  
48 maximum global 3-month average effective radiative forcing of -2 and -3 W/m<sup>2</sup>,  
49 respectively (Schmidt et al., 2018). After a period of low volcanic influence on the  
50 stratosphere around the turn of the millennium, many volcanic eruptions and wildfires  
51 have affected the aerosol in the stratosphere. The most important are the 2019-20  
52 Australian wildfires and the eruptions of Sarychev (2009), Raikoke (2019) and Hunga  
53 Ha’apai (2022).

54 Fresh wildfire aerosol particles contain black carbon and a dominating fraction of  
55 organics (Garofalo et al., 2019), where the latter is rapidly lost (half-life 10 days) in the  
56 stratosphere due to photolysis (Martinsson et al., 2022). The composition of volcanic  
57 stratospheric aerosol particles varies. SO<sub>2</sub>-rich volcanic emissions, like the 2008

58 eruption of Kasatochi, are dominated by sulfate, some organics and a minor fraction of  
59 ash (Martinsson et al., 2009, Andersson et al., 2013; Friberg et al., 2014). On the other  
60 hand, SO<sub>2</sub>-poor eruptions, like that of Puyehue-Cordón Caulle in 2011, are dominated  
61 by ash (Clarisse et al., 2013). Steam-boosted eruptions of submarine volcanoes (Mastin  
62 et al., 2024), like the 2022 eruption of Hunga Ha’apai, can result in a stratospheric  
63 aerosol with a strong contribution from sea salt (Martinsson et al., 2025).

64 From the beginning of extensive satellite data in the late 1970s the stratospheric aerosol  
65 load has usually been measured using solar occultation (Sato et al., 1993). GloSSAC  
66 (Global Space-based Stratospheric Aerosol Climatology), a later construction of a  
67 continuous record of optical properties of stratospheric aerosol spanning 1979 to  
68 present, has a core of solar occultation measurement with the notable 22 year era of  
69 SAGE II continuing a few years of solar occultation measurement by SAM II and SAGE I  
70 (Thomason et al., 2018). Solar occultation became unavailable during 2005 – 2017. To  
71 continue the GloSSAC record, other satellite-based measurements were deployed. The  
72 limb scatter instrument OSIRIS (Rieger et al., 2015) and the lidar CALIOP (Cloud-Aerosol  
73 Lidar with Orthogonal Polarization) (Winker et al., 2010) were, after substantial  
74 recalibration (Thomason et al., 2018, Kovilakam et al., 2020, Kovilakam et al., 2023),  
75 used to bridge the gap to obtain continuous time series of stratospheric aerosol  
76 properties. Mixing data from many sources that are relying on different measurement  
77 principles is however complex, as pointed out by Thomason et al. (2018). We will  
78 discuss this matter further in section 4.4.

79 This work deals with the stratospheric aerosol in the CALIOP era, spanning the 17-year  
80 period 2006-06-12 to 2023-06-30. CALIOP data (level 1B, version 4-51) is corrected for  
81 attenuation, and the lidar ratio is estimated for the stratospheric aerosol resulting from  
82 12 volcanic eruptions and wildfires. The stratosphere from the tropopause to 35 km  
83 altitude is divided into three altitude and three latitude parts, in total nine parts, where  
84 the backscattering of the background stratospheric aerosol is identified and its sources  
85 discussed. By subtraction of the signal from the background aerosol, the backscattering  
86 from major stratospheric aerosol events is obtained. This is converted to AOD using the  
87 estimated lidar ratios. We find that global average aerosol backscattering intensity on  
88 exceeded the background by 55% in the 17 years studied. The strongest influence from

89 volcanism and wildfires was in 2022 and 2023 due to the submarine Hunga Ha’apai  
90 eruption. The second strongest occurred in 2020 due to the Australian wildfires,  
91 followed by 2009 (Sarychev eruption) and 2019 (mainly the Raikoke eruption). 2013 was  
92 a year when the entire stratosphere was close to background conditions. Finally, we  
93 discuss the validity of lidar data in comparison with the more established data based on  
94 solar occultation.

## 95 **2. Methods**

96 This paper is based on measurements with the CALIOP lidar instrument aboard the  
97 CALIPSO (Cloud-Aerosol Lidar and Infrared Pathfinder Satellite Observation) satellite  
98 that completed approximately 15 orbits between latitudes -82 and 82° each day.

### 99 ***2.1 CALIOP properties and methods applied***

100 CALIOP with a laser of 532 nm wavelength produced vertical profiles of backscattering  
101 intensity from air molecules, aerosol particles and cloud drops from the ground up to 35  
102 km altitude with high vertical resolution depending on altitude. In the altitude ranges <  
103 8.2, 8.2 - 20.2, 20.2 – 30.1 and >30.1 km the vertical resolution is 30, 60, 180 and 300 m,  
104 respectively (Winker et al., 2007, 2010). Here we use data only from the stratosphere,  
105 where the tropopause altitude according to MERRA-2 reanalysis (Modern-Era  
106 Retrospective analysis for Research and Applications) (Gelaro et al., 2017) was used to  
107 discriminate data from the troposphere. Only data recorded during nighttime were used  
108 in the general evaluation concerning all the CALIOP data available (Friberg et al., 2018;  
109 Martinsson et al., 2022), implying that data will be missing at high latitudes for part of  
110 the year with the strongest influence at the summer solstice. The data were  
111 extrapolated linearly to cover all the way to 80° latitude in both hemispheres. The  
112 uncertainties in the global perspective used here are minor due to the small fraction of  
113 the surface area of the earth affected by the extrapolation.

114 The evaluation is based on version 4-51 of CALIOP level 1B data (NASA/LARC/SD/ASDC,  
115 2024). Clouds within 3km above the tropopause were discriminated based on  
116 depolarization of the signal obtained from the CALIOP instrument, polar stratospheric  
117 clouds were discriminated based on temperature and data taken in the South Atlantic

118 Anomaly are filtered out as explained in Friberg et al. (2018) and Martinsson et al.  
119 (2022). The backscatter data were corrected for attenuation by methodology described  
120 in Martinsson et al. (2022) and were first converted to extinction by the standard  
121 effective lidar ratio  $S = 50$  sr used for CALIOP (Kar et al., 2019). Volcanic eruptions and  
122 wildfires with lidar ratio deviating from 50 sr by more than 5% were corrected, see  
123 sections 2.3 and 4.2.

124 The stratospheric CALIOP level 3 product (Kar et al., 2019) and the data presented here  
125 are both based on the CALIOP level 1B data set but differ with respect to latitude-,  
126 longitude- and time-resolution, where CALIOP level 3 is based on monthly averages and  
127 we normally use a time-resolution of 1 – 8 days depending on issue investigated. These  
128 data sets also differ in with respect to lidar ratios: CALIOP level 3 extinction is obtained  
129 based on a fixed lidar ratio of 50 sr, whereas we, when possible, estimate effective lidar  
130 ratios for aerosol from individual volcanic eruptions and wildfires as described in  
131 sections 2.3, 3.1 and 4.2. The notion “effective” relates to that CALIOP is affected by  
132 multiple scattering, implying that use of lidar ratios for measurements unaffected by  
133 multiple scattering, i.e., the true physical relation between extinction and  
134 backscattering of the aerosol studied, will result in overestimation the extinction (Prata  
135 et al., 2017; Martinsson et al., 2022). Another difference between CALIOP level 3 and  
136 our method is that we correct data for attenuation of the detected scattered light  
137 (Martinsson et al., 2022), which is important for identification and quantification of  
138 aerosol processes in wildfire aerosol (Martinsson et al., 2022; Friberg et al., 2023) and  
139 volcanic aerosol (Martinsson et al., 2025) and to obtain the AOD without influence from  
140 attenuation.

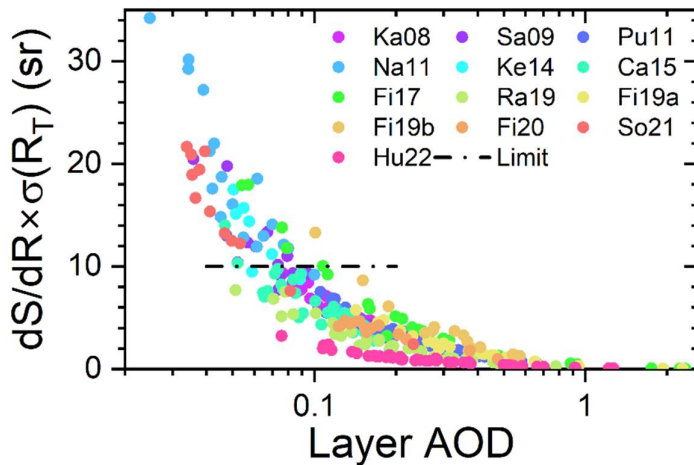
## 141 ***2.2 Estimation of the stratospheric background***

142 The stratospheric aerosol background can rarely be observed in the entire stratosphere.  
143 The last time the stratosphere was practically unaffected by injections from volcanic  
144 eruptions and wildfires for several years was a few years around the turn of the  
145 millennium (Solomon et al., 2011). Still, we need to find means to estimate the  
146 stratospheric background because we can estimate the lidar ratio of stratospheric  
147 injections from volcanic eruptions and wildfires (presented in next section) but not for  
148 the background aerosol. Injections from aerosol events seldom affect the entire

149 stratosphere. Therefore, parts of the stratosphere can be in background conditions  
150 when other parts are affected by aerosol injections.

151 To study the background conditions, the stratosphere was subdivided into nine parts  
152 spanned by three altitude layers: the lowermost stratosphere (LMS, from the  
153 tropopause to the 380 K isentrope, where the latter was obtained from MERRA-2  
154 pressures and temperatures), the shallow Brewer-Dobson branch (sBD, between  
155 isentropes 380 and 470 K) and the deep Brewer-Dobson branch (dBD, from the 470 K  
156 isentrope to 35 km altitude), and three latitude regions: the Southern extratropics  
157 (latitudes -80 to -20°), the tropics (latitudes -20 to 20°) and the Northern extratropics  
158 (latitudes 20 to 80°)., Data were averaged over 8 days resulting in 46 observations per  
159 year in each of the nine stratospheric parts. To estimate the background conditions in  
160 this 17-year study, the averages of the three years with the lowest average  
161 backscattering of each 8-day period were formed. For two of the nine stratospheric  
162 parts, the tropical sBD and dBD, background conditions were rare, wherefore only the  
163 two lowest years were used in these two stratospheric parts. The method applied  
164 results in the minimum concentration observed during the 17-year period. This means  
165 that in addition to the tropospheric aerosol and precursor gases entering the  
166 stratosphere across the tropical tropopause in the large-scale stratospheric circulation,  
167 phenomena such as the ATAL (Vernier et al., 2015) and other exchanges across the  
168 extratropical tropopause are included in the background.

169 The extracted lowest 8-day values formed a seasonal pattern that was fitted by the sum  
170 of a constant and a sinusoidal function. These fits were used to express the average  
171 backscattering of the background aerosol in each of the nine stratospheric parts over  
172 the 17 years spanned by CALIOP measurements. The average backscattering converts  
173 to AOD when multiplied with the lidar ratio. The fitted background was subtracted from  
174 the measured total backscattering to form the backscattering from volcanic eruptions  
175 and wildfires. These background-subtracted average backscattering data were  
176 converted to AOD via the lidar ratios obtained from individual aerosol events, as  
177 described in the next section.



178

179 **Figure 1.** Relation between the layer AOD and the measure on the uncertainty of the  
 180 lidar ratio estimation.  $dS/dR$  is the sensitivity of the lidar ratio ( $S$ ) to small shifts of the  
 181 target scattering ratio ( $R$ ) and  $\sigma(R_T)$  is the standard deviation of the target  $R$  of each  
 182 eruption or wildfire obtained horizontally beside each aerosol layer investigated. Layers  
 183 with uncertainty exceeding 10 sr (“limit”) are discarded in the following analysis.

### 184 **2.3 Lidar ratio**

185 The lidar ratio of the aerosol from the strongest volcanic eruptions and wildfires in the  
 186 period studied was estimated based on methodology described in Martinsson et al.  
 187 (2022), where individual dense aerosol layers are investigated. In that method a target  
 188 value in scattering ratio ( $R$ ) obtained horizontally beside the studied aerosol layer ( $R_T$ ) is  
 189 reached below the layer in an iterative procedure that results in an estimate of the  
 190 effective lidar ratio, while correcting for attenuation of the backscattered signal. The  
 191 effective lidar ratio obtained describes the average conditions of the entire layer where  
 192 the optical properties in principle can vary. However, the lidar ratio estimates are  
 193 obtained in dense aerosol layers, where the influence from background aerosol is small.

194 The uncertainty in the estimated lidar ratio depends on the AOD of the layer. A small  
 195 change in the lidar ratio ( $S$ ) results in a substantial change in the scattering ratio ( $R$ )  
 196 below a dense layer, i.e.,  $dS/dR$  is small for dense aerosol layers.  $dS/dR$  is obtained by  
 197 shifting  $R$  slightly around  $R_T$ . There is also an uncertainty in how well  $R_T$  represents the  
 198 aerosol beneath the layer. We estimate that uncertainty by the standard deviation of the  
 199 scattering ratio ( $\sigma(R_T)$ ) obtained horizontally beside all the aerosol layers studied for

200 each volcanic eruption or wildfire. This is thus based on the assumption that the aerosol  
201 horizontally beside and below the aerosol layer have the same standard deviation in  $R$ ,  
202 but the actual scattering ratios horizontally beside and below an individual layer are  
203 uncorrelated. The estimated uncertainty becomes  $dS/dR \times \sigma(R_T)$ . Figure 1 shows all  
204  $dS/dR \times \sigma(R_T)$  related to the AOD of all the estimations of the lidar ratio. The uncertainty in  
205 the lidar ratio estimate increases as the layer AOD decreases, hence a limit was set to  
206  $dS/dR \times \sigma(R_T) < 10$  sr to pass as a lidar ratio estimate. As a result, most estimates for  
207 three volcanic eruptions, 2011 Nabro (Na11), 2014 Kelut (Ke14), and 2021 Soufriere  
208 (So21), among the 12 eruptions and wildfires analyzed were lost, as illustrated in Figure  
209 1.

210 For simplicity all the CALIOP data were evaluated using the standard lidar ratio of  $S_0 =$   
211 50 sr in the general evaluation. In the study of individual aerosol layers (Figure 1) both  
212 the AOD based on the estimated lidar ratio and that based on  $S_0$  were computed, where  
213 the latter ( $AOD_{S_0}$ ) was used to obtain the deviation caused by using  $S_0$ . This deviation  
214 depends on the  $S/S_0$  ratio and  $AOD_{S_0}$ , where the effect of  $S/S_0$  is the dominant one  
215 except for very dense aerosol layers. The result from the general evaluation is corrected  
216 afterwards based on the difference between  $S_0$  and the estimated  $S$ , see section 4.2.

### 217 **3. Results**

218 Here we will present the stratospheric aerosol from the troposphere to 35 km altitude  
219 and the latitude range  $-80$  to  $80^\circ$  in the era of lidar measurements by the CALIOP  
220 instrument aboard the CALIPSO satellite. CALIOP measured the backscattered intensity  
221 from a 532 nm laser beam, which can be converted to extinction by multiplying with the  
222 ratio of extinction to backscatter, i.e. the lidar ratio. Knowing the lidar ratio thus is  
223 central for quantification by obtaining AOD from CALIOP measurements. We developed  
224 methodology to estimate the effective lidar ratio from CALIOP measurements, a  
225 methodology that also corrects for attenuation of the laser signal (Martinsson et al.,  
226 2022). Here we start by presenting the lidar ratio of the main aerosol events of the  
227 CALIOP era before giving an overview of the AOD in the period studied.

#### 228 **3.1 Lidar ratio**

229 The main aerosol events affecting the stratosphere in the CALIOP era are presented in  
 230 Table 1. The methodology we use to estimate lidar ratios requires sufficiently dense  
 231 aerosol layers as described in section 2, implying that some of the events mentioned in  
 232 Table 1 are not suitable for the methodology. The lidar ratio was investigated for

233 **Table 1.** Major volcanic eruptions and wildfires affecting the stratospheric aerosol in the  
 234 CALIOP era.

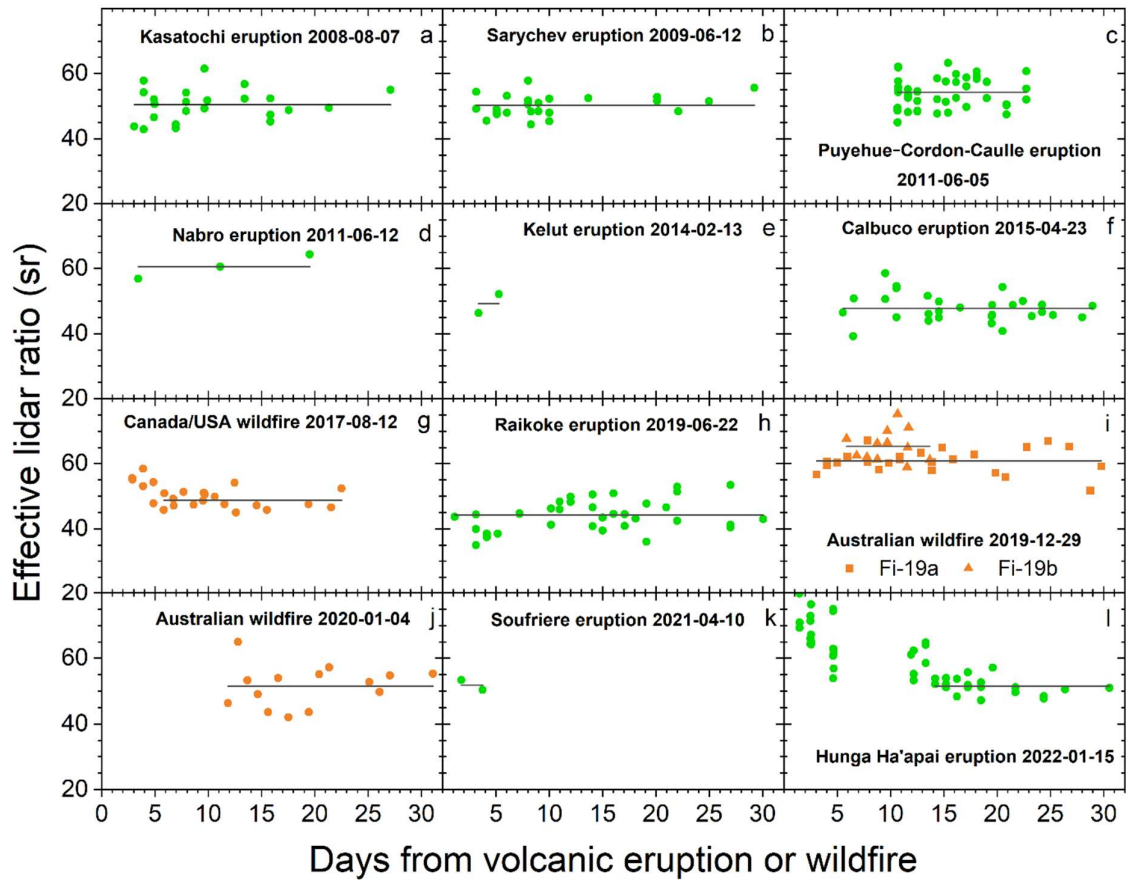
	Date	Volcano/wildfire	Lat <sup>a</sup>	Lon <sup>b</sup>	SO <sub>2</sub> (Tg)	References
	<i>Volcanic eruptions</i>					
1	2006-05-20	Soufriere Hills (Su)	17°	-62.2°	0.2	Carn and Prata (2010)
2	2006-10-07	Rabaul (Rb)	-4°	152°	0.23	Carn et al. (2009)
3	2008-08-07	Kasatochi (Ka)	52°	-176°	1.7	Thomas et al. (2011)
4	2009-06-12	Sarychev (Sa)	48°	153°	1.2	Haywood et al. (2010)
5	2010-10-05	Merapi (Me)	-7°	110°	0.44	Surono et al. (2012)
6	2011-06-05	Puyehue-Cordón Caulle (Pu)	-40°	-72°	0.25	Clarisse et al. (2012)
7	2011-06-12	Nabro (Na)	13°	42°	1.5	Clarisse et al. (2012)
8	2014-02-13	Kelut (Ke)	-8°	112°	0.18	Li et al. (2017)
9	2015-04-23	Calbuco (Ca)	-41°	-73°	0.3	Pardini et al. (2018)
10	2018-07-27	Ambae (Am)	-15°	168°	0.36	Malinina et al. (2021)
11	2019-06-22	Raikoke (Ra)	48°	153°	1.5	Kloss et al. (2021)
12	2019-06-26	Ulawun (Ul)	-5°	151°	0.14	Kloss et al. (2021)
13	2019-08-03	Ulawun (Ul)	-5°	151°	0.3	Kloss et al. (2021)
14	2021-04-10	Soufriere (So)	13°	-61°	0.31	Taylor et al. (2023)
15	2022-01-15	Hunga Ha'apai (Hu)	-21°	175°	0.45	Carn et al. (2022)
	<i>Wildfires</i>					
16	2006-12-19	Australia (A1)	-37°	147°	-	McCarthy et al. (2012)
17	2009-02-07	Australia (A2)	-38°	146°	-	Cruz et al. (2012)
18	2017-08-12	Canada/USA (CU)	53°	-123°	-	Fromm et al. (2021)
19	2019-12-29	Australia (A3)	-37°	149°	-	Peterson et al. (2021)
20	2020-01-04	Australia (A4)	-37°	149°	-	Peterson et al. (2021)

235

236 stratospheric aerosol from nine volcanic eruptions and three wildfire events (Figure 2).  
 237 For some of these aerosol events the screening related to the uncertainty in the  
 238 estimated lidar ratio (Figure 1) resulted in few observations, namely for the 2011 Nabro,  
 239 2014 Kelut and the 2021 Soufriere eruptions. Most of the eruptions and wildfires display  
 240 a stable lidar ratio during the first month, whereas two of the events show an initial  
 241 decrease of the lidar ratio, the 2017 North American wildfire (Figure 2g) and the 2022  
 242 Hunga Ha'apai eruption (Figure 2l), towards a stable value.

243 Effective lidar ratios are presented here which are best suited for application to  
244 measurements that, like CALIOP, are affected by multiple scattering (Martinsson et al.,  
245 2022). Compared with previous estimates, the results presented here are approximately  
246 20% lower than those of Prata et al. (2017) for the Kasatochi, Sarychev and Puyehue-  
247 Cordon Caulle eruptions, who estimated lidar ratio for measurements that are not  
248 affected by multiple scattering. Ohneiser et al. (2020) present Raman lidar measurements of  
249 the 2019 Australian wildfire (Table 1) that are not affected by multiple scattering. On 2020-01-09  
250 around 04:00 UTC (longitude -70.9, latitude -53.2)  $S = 76$  sr was obtained. The closest CALIOP  
251 measurement in space and time that we evaluated was taken on the same day at 04:05,  
252 position (-43.4, -53.1) with  $S = 75$  sr. The day before, at position (-57.2, -50.0)  $S = 70$  sr and the  
253 day after at position (-55.0, -57.1)  $S = 71$  sr. All these three measurements belong to the fires  
254 taking place last days of 2019, category B (outside the vortex) and are the three highest effective  
255 lidar ratios obtained in this category.

256 Stratospheric aerosol resulting from most volcanic eruptions and wildfires have a lidar  
257 ratio close to 50 sr, which is the commonly used lidar ratio for CALIOP data (Kar et al.,  
258 2019). Notable exceptions with lidar ratio deviating by more than 5% from 50 sr are the  
259 ash-dominated 2011 eruption of Puyehue-Cordón Caulle (Figure 2c), the 2019



260

261 **Figure 2.** Effective particle lidar ratios the first 30 days after a volcanic eruption or  
 262 wildfire with a line displaying the average of each event. All measurements concurring  
 263 with the condition  $dS/dR \times \sigma(R) < 10$  are displayed for a) Kasatochi eruption 2008-08-07,  
 264 b) Sarychev eruption 2009-06-12, c) Puyehue-Cordón-Caulle eruption 2011-06-05, d)  
 265 Nabro eruption 2011-06-12, e) Kelut eruption 2014-02-13, f) Calbuco eruption 2015-04-  
 266 23, g) Canada/USA wildfire 2017-08-12, h) Raikoke eruption 2019-06-22, i) Australian  
 267 wildfire, 2019-12-29 subdivided in part Fi-19a (observations in the vortex (Kablik et al.,  
 268 2020)) and Fi-19b (observations outside the vortex), j) Australian wildfire 2020-01-04, k)  
 269 Soufriere eruption 2021-04-10 and l) Hunga Ha'apai eruption 2022-01-15. The averages  
 270 include all data points except for the Canada/USA wildfire and the Hunga Ha'apai  
 271 eruption where the initial decline in the lidar ratio is not part of the average represented  
 272 by horizontal lines.

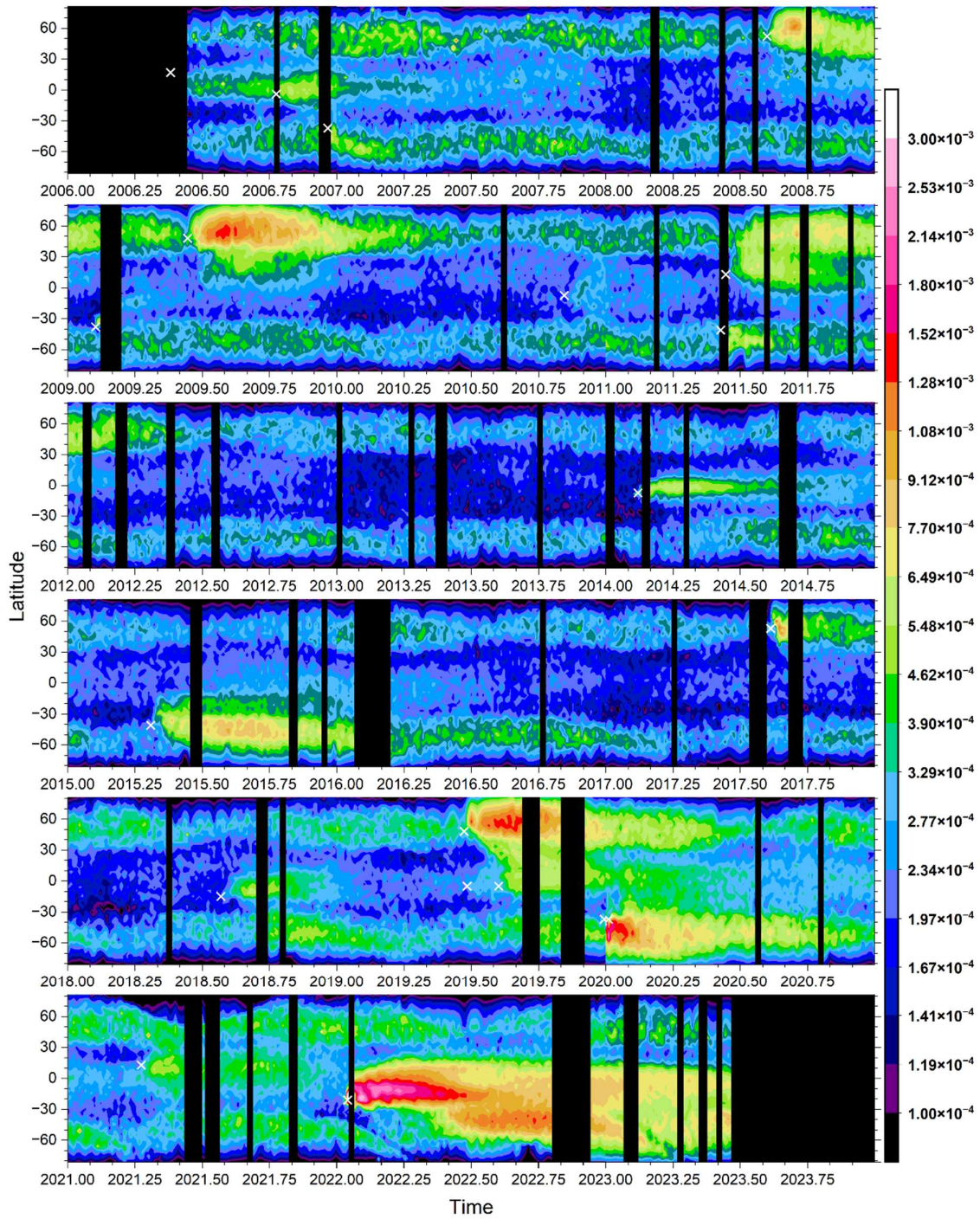
273

274 Raikoke eruption (Figure 2h) and the Australian wildfire in the last days of 2019 (Figure  
275 2i). Also, the 2011 Nabro eruption (Figure 2d) tends to deviate from the commonly  
276 adopted lidar ratio of 50 sr of stratospheric aerosol, however the observations are too  
277 few for a firm conclusion. In the forthcoming presentation the lidar ratio of 50 sr will be  
278 used before a discussion on the influence from deviations is addressed in sections 4.2  
279 and 4.3.

### 280 **3.2 Stratospheric aerosol events overview**

281 At least 15 volcanic eruptions and 5 wildfires clearly affected the stratospheric aerosol  
282 in the CALIOP era (Table 1). The latitude distribution of the stratospheric aerosol from  
283 the tropopause to 35 km altitude is shown in Figure 3, and subdivided into three layers,  
284 dBD, sBD, and LMS, in Figures S1 – S3. Additionally, the altitude distribution is shown in  
285 three latitude ranges (Figures S4 – S6).

286 The influence from injections of aerosol from volcanic eruptions and wildfires has  
287 durations of a few months to several years (Friberg et al., 2018). The latter category is  
288 the aerosol events that enter the dBD branch in the tropics. The outstanding event  
289 fulfilling this requirement in the period studied is the submarine eruption of Hunga  
290 Ha’apai in 2022 (Figures S1 and S5) where intense volcanism – sea interaction  
291 (Seabrook et al., 2023; Mastin et al., 2024) formed large quantities of stratospheric  
292 aerosol (Martinsson et al., 2025). The remaining aerosol events in the dBD have much  
293 lower AODs. The Kelut eruption in 2014 affected the dBD for approximately 4 years, the  
294 combined effect of the 2006 eruptions of Soufriere Hills and Rabaul (Figure S5) show  
295 similar long-term effects on the dBD in the tropics (Figure S1). The combined effects of  
296 4 volcanic eruptions, the 2018 Ambae, the two 2019 Ulawun and the 2021 Soufriere  
297 eruptions, gradually increased the dBD aerosol concentration in the tropics. In addition  
298 to these tropical eruptions, some extratropical aerosol events affected the dBD: the  
299 2015 Calbuco eruption and some overshooting plumes reaching above the main  
300 effluents of the 2019 Raikoke eruption. Three wildfires also contributed aerosol to the  
301 extratropical dBD, the 2009 Australian, the 2017 Canada/USA and the 2019 Australian  
302 wildfires. The aerosol from the latter fire formed a vortex where the aerosol rose above  
303 31 km altitude (Kablick et al., 2020). The extratropical aerosol events leave the dBD



304

305 **Figure 3.** AOD integrated from the tropopause to 35 km altitude averaged over 4 days  
 306 and 3 degrees in latitude. The lidar ratio is set to 50 sr. Color scale: Global AOD  
 307 contribution per degree of latitude, i.e. the sum over latitude is the total AOD at any  
 308 given time. White crosses indicate time and latitude of aerosol events mentioned in  
 309 Table 1.

310

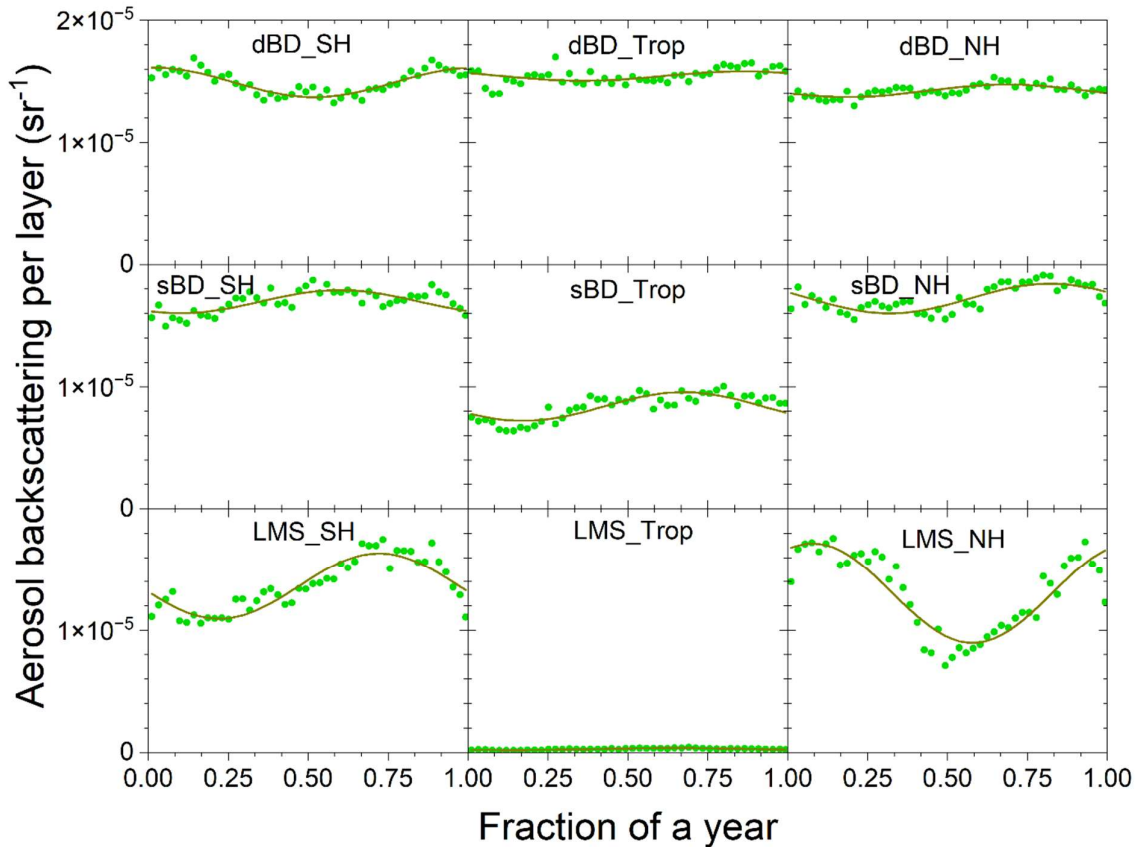
311 faster than the tropical ones because of the extratropical downward motion of the BD  
312 circulation.

313 The shallow Brewer-Dobson (sBD) branch displays no such strong aerosol event as the  
314 effect of the 2022 Hunga Ha'apai eruption on the dBD (Figure S2). On the other hand,  
315 many events had intermediate or small impacts. The Australian wildfires at the end of  
316 2019 and the beginning of 2020 made an initial strong impact that rapidly (half-life 10  
317 days) lost 90% of the aerosol likely due to photolysis of organic aerosol (Friberg et al.,  
318 2023), as did the 2017 North American wildfire but with a lower aerosol load  
319 (Martinsson et al. 2022) and, to a still lower extent, the 2009 Australian wildfire. The  
320 main volcanic eruptions affecting the sBD branch were the 2008 Kasatochi, 2009  
321 Sarychev, 2011 Nabro, 2015 Calbuco, 2019 Raikoke and, after a delay due to transport  
322 from the dBD branch, the 2022 Hunga Ha'apai eruptions. Other volcanos with smaller  
323 impact on the sBD branch were the 2006 Soufriere Hills and Rabaul, the 2010 Merapi,  
324 2014 Kelut, 2018 Ambae, 2019 Ulawun (2 eruptions) and 2021 Soufriere eruptions.

325 The LMS, the last passage for air and its trace substances in the large-scale  
326 stratospheric circulation before exiting to the troposphere, is affected by all  
327 stratospheric aerosol events. In addition, some extratropical aerosol events do not  
328 reach beyond the LMS. The Kasatochi eruption resulted in two distinct aerosol layers, a  
329 thin layer in the sBD whereas the main part of its effluents was injected both sides of  
330 and close to the tropopause (Andersson et al., 2015). Other exclusive LMS events in the  
331 period studied here are the 2011 Puyehue-Cordón Caulle eruption and the 2006  
332 Australia wildfire.

333 Most volcanic eruptions show a gradual increase in AOD over few months before  
334 reaching its maximum because of the time required for aerosol dynamical processing  
335 and to transform sulfur dioxide into sulfate, which usually is the main component of the  
336 aerosol from volcanic eruptions. Notable exceptions are the 2022 Hunga Ha'apai and  
337 the 2011 Puyehue-Cordón Caulle eruptions (Figure 2). The aerosol of the latter eruption  
338 mainly consisted of volcanic ash (Vernier et al., 2013) and the former by aerosol  
339 containing sulfate and sea-salt from volcanism – sea interaction (Martinsson et al.,  
340 2025). These eruptions are thus less influenced by delay in aerosol formation from  
341 chemical transformation. The wildfires in the years 2009, 2017, 2019 and 2020 also

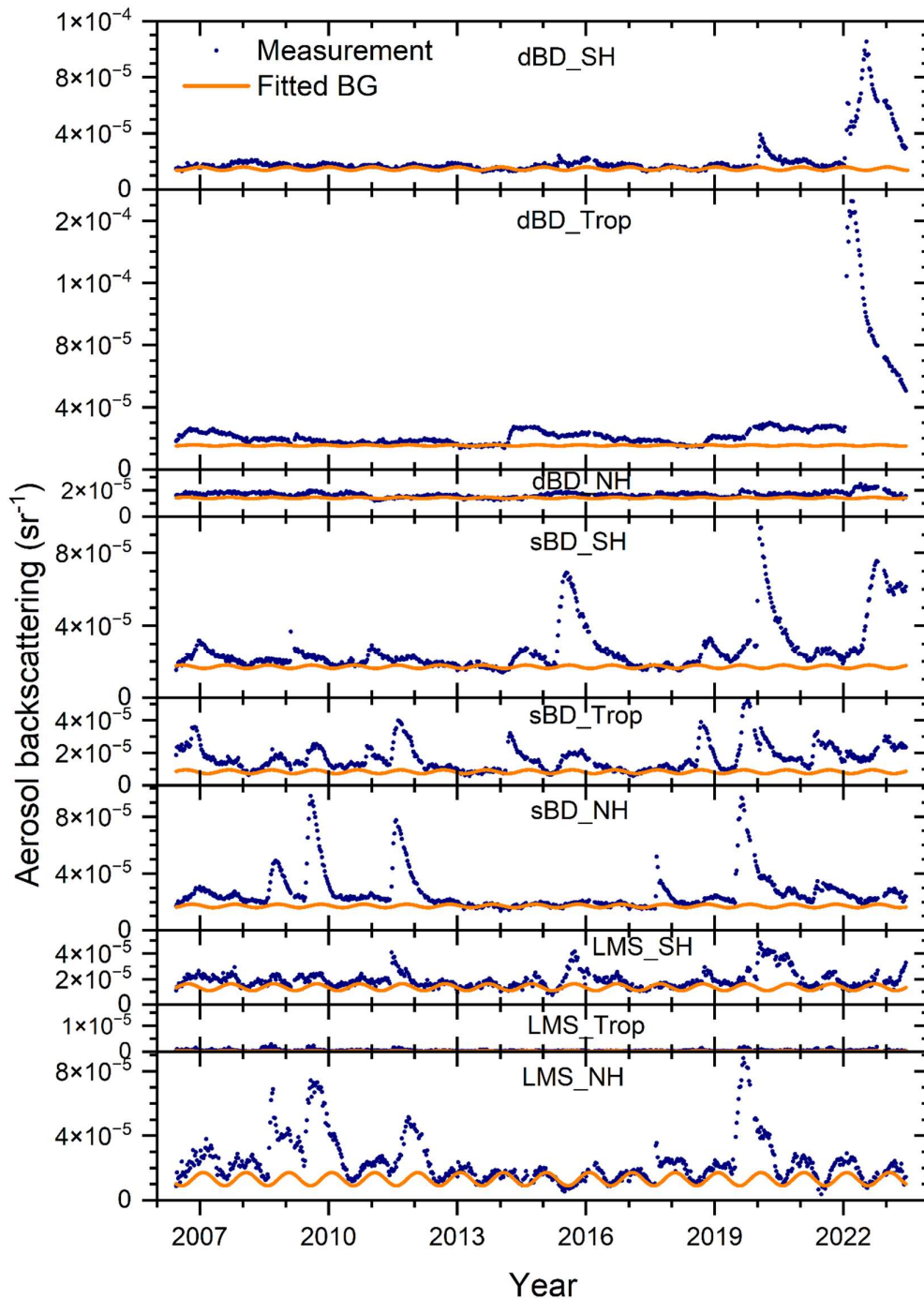
342 rapidly reach the maximum AOD before a decline due to photolysis of organic  
 343 compounds with a half-life of ten days reduces the AOD by 90% (Martinsson et al.,  
 344 2022; Friberg et al., 2023).



345  
 346 **Figure 4.** Average backscattering, which when multiplied with the lidar ratio becomes  
 347 the AOD of the layer, of the background aerosol extracted based on the three lowest  
 348 average values of each 8-day period over the year in the CALIOP era (2006 – 2023). The  
 349 extracted data were fitted to a constant and a sinusoidal function. (Exceptions: the two  
 350 lowest 8-day averages were used for “dBD\_Trop” and “sBD\_Trop” due to infrequent  
 351 background values.) The extraction was undertaken in nine regions spanned by  
 352 latitudes: -80 to -20° (SH), -20 to 20° (Tropics), 20 to 80° (NH) and altitude ranges: the  
 353 tropopause to 380 K isentrope (LMS), 380 to 470 K isentrope (sBD), 470 K to 35 km  
 354 altitude (dBD). The data were latitude weighted in the way that the sum of the nine  
 355 layers is the global aerosol backscattering.

### 356 4. Discussion

357 We discuss separation of aerosol signals of aerosol events due to volcanic eruptions  
 358 and wildfires from signals due to stratospheric background aerosol. This is followed by  
 359 sections on corrections of AOD due to lidar ratio deviations from the commonly



360

361 **Figure 5.** Stratospheric aerosol average backscattering, which when multiplied with the  
 362 lidar ratio becomes the AOD, and fitted background in nine latitude and altitude regions:  
 363 the deep BD branch (470 K isentrope to 35 km altitude), the shallow BD branch  
 364 (between isentropes 380 and 470 K) and the LMS (from the tropopause to the 380 K  
 365 isentrope) and three latitude regions the southern hemisphere extratropics (-80 to -20°),  
 366 the tropics (-20 to 20°) and the northern hemisphere extratropics (20 to 80°) to find time-  
 367 sections not or weakly affected by stratospheric aerosol events (see Fig. 4 and text for  
 368 details).

369 assumed 50 sr. Then we overview the AOD and climate impact and, finally, discuss the  
370 validity of AODs from CALIOP relative to solar occultation-based instruments.

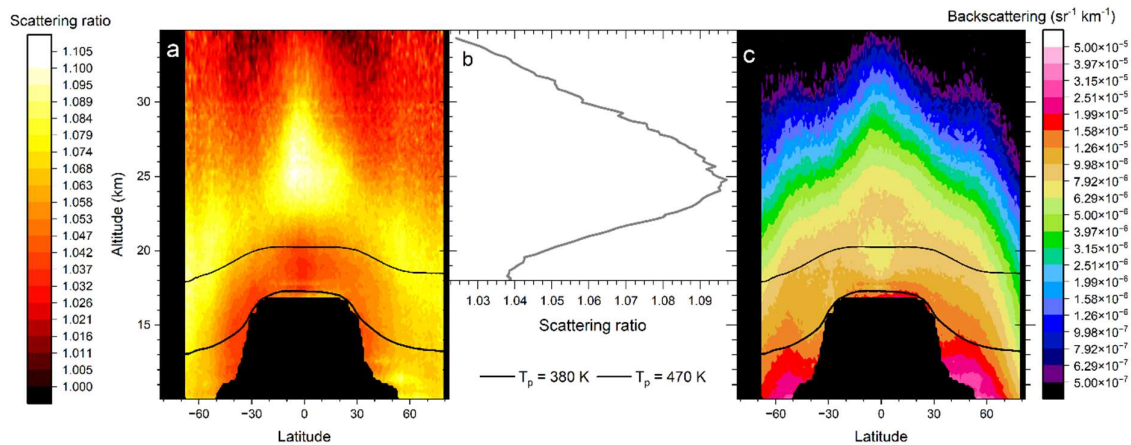
#### 371 **4.1 Stratospheric background**

372 The stratospheric background aerosol is not a well-defined concept. One way is to  
373 include all but major aerosol events in the background to obtain a persistently variable  
374 background (Solomon et al., 2011). An alternative background is based on SAGE II  
375 measurements in the volcanically quiescent period in the late 1990s to early 2000s  
376 (Kremser et al., 2016). CALIOP measurements were not available in those years. A  
377 volcanic eruption or wildfire rarely affects the entire stratosphere. Therefore, we divided  
378 the stratosphere into nine sections by altitude and latitude thereby increasing the  
379 probability of finding conditions close to background separately in each of the layers  
380 using the average of the three lowest average backscattering values (in two cases the  
381 two lowest) of each layer over the year (Figure 4), as described in the methods section.

382 The distribution of aerosol over the nine layers used to extract the background aerosol is  
383 shown in Table 2. Seven of the nine layers each contain 11 – 15% of the background  
384 aerosol in the stratosphere from the tropopause to 35 km altitude during conditions that  
385 are close to background. The smallest contribution comes from the tropical LMS, which  
386 is to be expected given the small air volume of that layer. The tropical sBD also has a  
387 small contribution, but that cannot be explained by the air volume. This layer where  
388 tropospheric air enters the stratosphere extends to approximately 20 km altitude, where  
389 UV radiation intensity is too weak to efficiently oxidize carbonyl sulfide (Weisenstein et  
390 al., 1997), which is an important precursor gas of the stratospheric background aerosol  
391 (Crutzen, 1976; Kremser et al., 2016), a topic we return to below. Seasonal changes in  
392 aerosol background average backscattering are most pronounced in the extratropical  
393 LMS, especially in the NH. The volume of LMS varies over the year. That variation  
394 (Appenzeller et al., 1996) approximately coincides with the variation in Figure 4 both in  
395 terms of seasonality and the stronger amplitude in the LMS of the NH. This is also  
396 connected to aerosol concentrations of the LMS. Poleward transport in the BD  
397 circulation maximizes in the winter resulting in increased extratropical downward  
398 motion of the stratospheric aerosol layer in the spring resulting in low aerosol load in the  
399 summer LMS when the mass transport across its upper boundary is at its minimum. The

400 latter also coincides with the weakening of the subtropical Jetstream which increases  
 401 the tropospheric influence on the LMS. In the summer/early fall there is also influence  
 402 from ATAL (Vernier et al., 2015) and small wildfires briefly affecting the stratosphere  
 403 (Peterson et al., 2025). The chemical composition of the LMS aerosol of the Northern  
 404 hemisphere in that period differs from winter/spring/early summer by having a larger  
 405 carbon than sulfur content (Martinsson et al., 2019). The change in composition can be  
 406 caused by the ATAL and/or small wildfires which thus contribute to the effect of the  
 407 large-scale stratospheric circulation in the build-up of the NH LMS aerosol load during  
 408 late summer and fall.

409 The average backscattering of the stratospheric aerosol and the estimated background  
 410 (Figure 4) in nine altitude and latitude layers is shown in Figure 5. By comparing these  
 411 two quantities, we verify the underlying assumption in the method used to obtain the  
 412 background that the stratospheric aerosol background has no long-term trend, which  
 413 agrees with previous observations (Kremser et al., 2016). Subtracting the background,



414

415 **Figure 6.** The stratospheric aerosol averaged over year 2013, which was close to  
 416 background conditions. a) The scattering ratio, i.e., the ratio between the total to the  
 417 modeled backscattering of air molecules. This intensive parameter is not latitude  
 418 weighted. b) Average scattering ratio in the central tropics (latitudes  $-10$  to  $10^\circ$ )  
 419 dependence on altitude. c) Average aerosol backscattering, this extensive quantity is  
 420 latitude weighted. Black lines in a) and c) are the yearly average positions of the  
 421 potential temperatures ( $T_p$ ) 380 and 470 K.

422

423 we obtain the average backscattering from volcanic eruptions and wildfires. The net  
 424 average backscattering of the layers was converted to AOD of the layers by  
 425 multiplication with the lidar ratio of 50 sr in Figure S7 with contributions from volcanic  
 426 eruptions and wildfires as described in section 3.2.

427 Except for a tiny peak in the LMS in the Northern extratropics, 2013 is close to  
 428 background conditions (Figure 5). The stratospheric background aerosol is often  
 429 thought of as a layer located above 20 km altitude in the tropics and lower in the  
 430 extratropics. This is approximately true in terms of scattering ratio (R), the optical  
 431 equivalent of mixing ratio (Figure 6a). More than half of the air entering the tropical  
 432 stratosphere is transported polewards in the sBD (Lin and Fu, 2013), where the  
 433 scattering ratio remains low in a band closest to the tropopause (Figure 6a). This band  
 434 contains young stratospheric air compared to air at the same altitude but at higher  
 435 latitude (Austin and Li, 2006; Butchart, 2014; Ploeger et al., 2021). In the air rising  
 436 further in the tropical stratosphere a dramatic increase of the aerosol mixing ratio can  
 437 be seen above 20 km altitude. The aerosol signal increases by a factor 2.5 (Figure 6b)  
 438 from 19 to 25 km altitude in the latitude range -10 to 10°, i.e., 70% of the aerosol at 25  
 439 km is formed above 19 km altitude. The dBD air is transported polewards and descends  
 440 at higher latitudes than the sBD air (Figure 6a). With a typical vertical

441 **Table 2.** Average backscattering of background aerosol and AOD of aerosol events in  
 442 2006 - 2023 and the distribution over nine stratospheric layers.

Backscattering background <sup>a</sup>				
	<i>Global</i>	SH	Tropics	NH
<i>Total</i>		40%	21%	39%
dBD	39%	13%	14%	12%
sBD	37%	15%	7.3%	15%
LMS	24%	12%	0.2%	11%
AOD aerosol events <sup>b</sup>				
	<i>Global</i>	SH	Tropics	NH
<i>Total</i>		33%	31%	35%
dBD	31%	9.0%	18%	4.0%
sBD	43%	15%	13%	15%
LMS	26%	9.0%	0.4%	17%

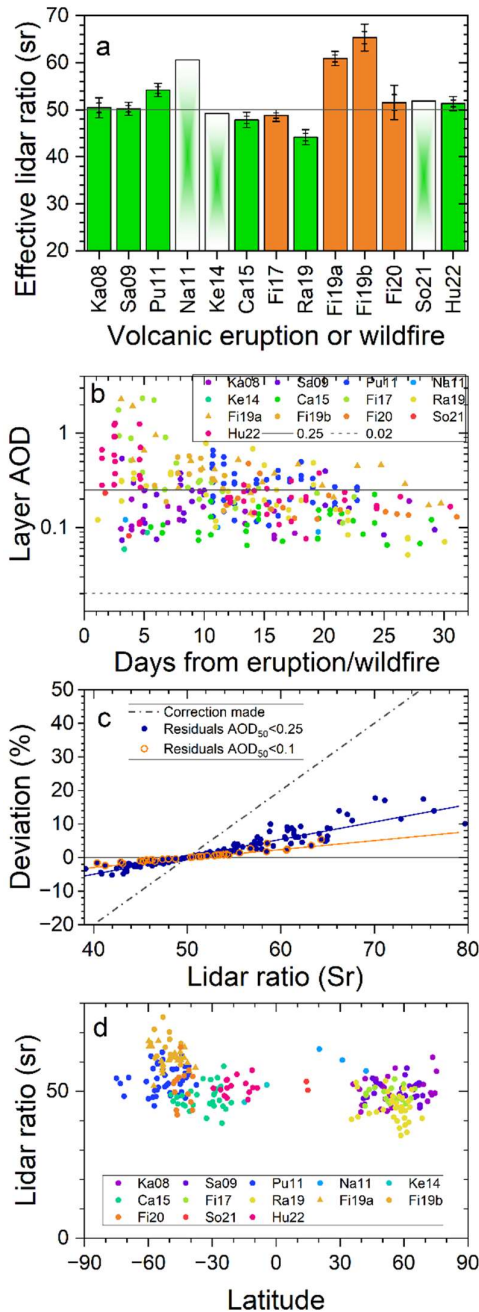
443 <sup>a</sup>Average backscattering of background = 0.00011 sr<sup>-1</sup>

444 <sup>b</sup>Average AOD from aerosol events (2006 – 2023) = 0.0031

445

446 velocity of 20 m/day (Mote et al., 1998) the transport from the tropical tropopause (at 17  
447 km) to 19 km altitude requires approximately 100 days, providing ample time for  
448 conversion of SO<sub>2</sub> before reaching the latter altitude (Nicknisch et al., 2025). Hence, little  
449 SO<sub>2</sub> enters the dBD, implying particle formation from another source. Intensifying UV  
450 radiation with altitude causes oxidation of the most abundant sulfur compound in the  
451 atmosphere, i.e., carbonyl sulfide (OCS) (Crutzen, 1976; Kremser et al., 2016), whereas  
452 this compound remains intact in the sBD. The requirement of intense UV radiation for  
453 oxidation makes OCS an important aerosol formation pathway mainly in the dBD. The  
454 formed aerosol is transported polewards where downward transport brings the aerosol  
455 to the sBD and LMS layers before the transport out of the stratosphere (Figure 6a). The  
456 formation pathways of the stratospheric background aerosol are still debated. The  
457 estimated contribution of OCS to the stratospheric background aerosol ranges from 20  
458 – 50% (Sheng et al., 2015; Chin and Davies, 1995) to 70% or more (Crutzen, 1976; Brühl  
459 et al., 2012). High-resolution lidar data, like that of CALIOP, can be used to constrain  
460 modeling efforts by reconstructing the CALIOP observations in Figure 6 to understand  
461 the sources of the background aerosol.

462 When instead considering the absolute background aerosol load (Figure 6c) we find the  
463 highest aerosol load at low stratospheric altitudes. The air in the Brewer-Dobson



464

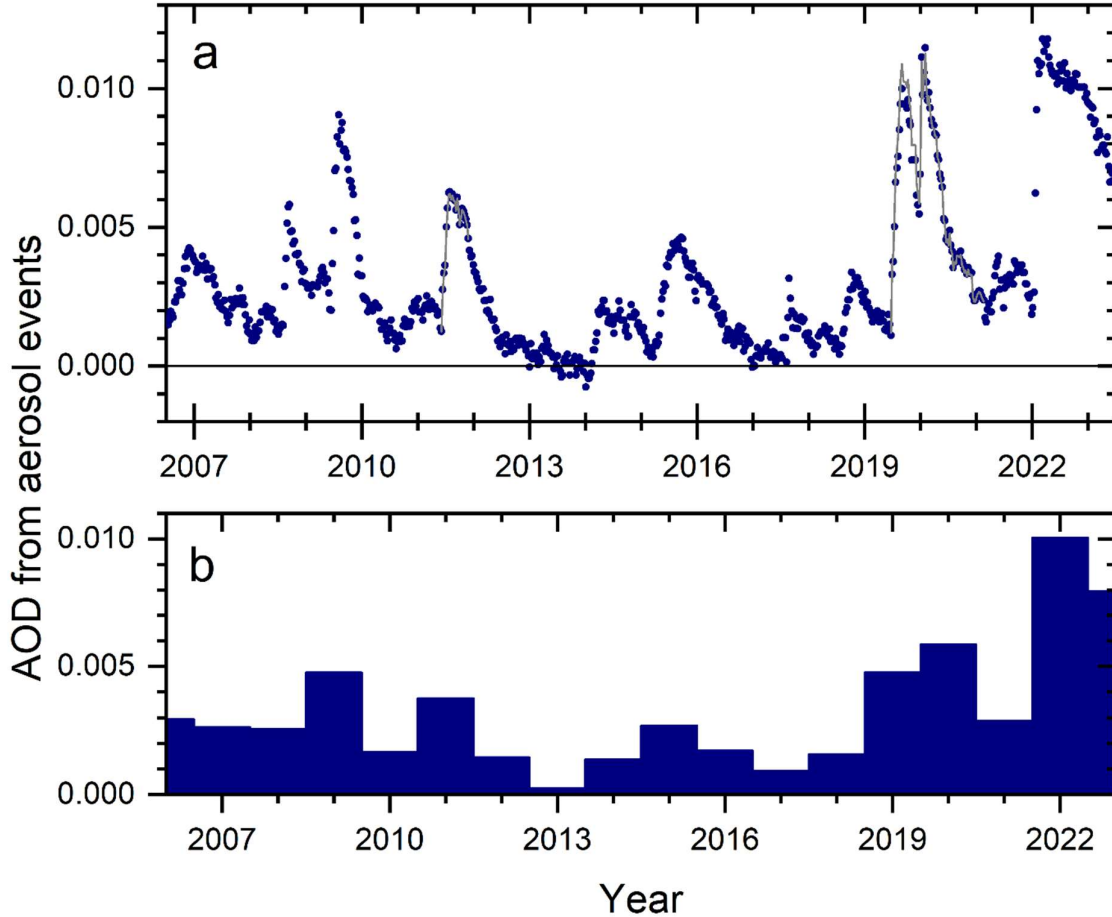
465 **Figure 7.** a) Average lidar ratios according to Fig. 2 with standard errors and 95% ranges  
 466 of volcanic eruptions and wildfires. Too few observations for error estimations were  
 467 obtained for the eruptions of Nabro (Na11), Kelut (Ke14) and Soufriere (So21). b) AODs  
 468 of aerosol layers with  $dS/dR \times \sigma(R) < 10$  sr Vs. time from the eruption or wildfire. The full  
 469 line illustrates approximate maximum layer AOD after 1 month, and the broken line  
 470 indicates the approximate maximum layer AOD observable by limb-viewing techniques  
 471 (note: logarithmic y-scale). c) Correction of AOD obtained by setting the lidar ratio to 50  
 472 sr ( $AOD_{50}$ ), based on a linear dependence of the AOD on the lidar ratio. The residual  
 473 deviation after the correction of two categories is also shown: aerosol layers with  $AOD_{50}$   
 474  $< 0.1$  and  $< 0.25$ . d) Estimated lidar ratios in Figure 2 Vs. latitude.

475 circulation becomes compressed during the downwelling in the extratropics in  
476 accordance with the altitude-dependence of the atmospheric pressure. During  
477 background conditions approximately 60% of the aerosol backscattering signal (AOD  
478 divided by the lidar ratio) is found in the two lower layers, sBD and LMS (Table 2),  
479 containing aerosol transported from both the sBD and dBD of the tropics.

#### 480 **4.2 Correction of lidar ratio**

481 Thus far we have presented AODs with the lidar ratio set to 50 sr. The lidar ratios of the  
482 individual measurements are shown in Figure 2. In Figure 7a we show the averages with  
483 statistical uncertainty (standard error and double-sided 95% confidence interval). As  
484 already pointed out, three of the eruptions (Nabro 2011, Kelut 2014 and Soufriere 2021)  
485 cannot be evaluated statistically due to few available measurements. Most of the  
486 aerosol events show lidar ratios of approximately 50 sr, whereas the aerosol from  
487 Puyehue-Cordón Caulle (2011), Raikoke (2019) and the Australian wildfires in the end of  
488 2019 deviates from 50 sr by more than 5%.

489 To convert the AOD obtained using  $S_0 = 50$  sr to the estimated lidar ratio ( $S$ ) we need to  
490 consider the linear dependence of the AOD on the lidar ratio. A secondary effect relates  
491 to the level of AOD. For the latter, we need to evaluate the occurrence of dense aerosol  
492 layers. All the measurements fulfilling the criteria on uncertainty of the lidar ratio  
493 estimate (Figure 1) are displayed in Figure 7b. Initially layer AODs sometimes exceed 1.  
494 After 20 days the AOD of the individual aerosol layers is mostly 0.25 and lower, except  
495 for the 2019 Australian wildfire that remain somewhat higher probably due to less air  
496 mixing in the vortex formed (Kablick et al., 2020). We corrected the AODs by  $S/S_0$  for  
497 volcanic eruptions and wildfires that formed an aerosol with effective lidar ratio  
498 deviating more than 5% from  $S_0 = 50$  sr, whereas the residual correction connected with  
499 the AOD of an aerosol layer was not accounted for (see the methods section for further  
500 detail) because the effect is small (Figure 7c). In the general evaluation we did not  
501 separate the aerosol backscattering from the 2019 and 2020 Australian wildfires that  
502 were only a few days apart. The 2020 fire was dominant in terms of AOD with 80 – 90%  
503 of the total AOD from the two fires (Friberg et al., 2023). Here, we weigh the lidar ratios  
504 of the two fires accordingly to obtain  $S = 53.3$  representing both fires.



506

507 **Figure 8.** Background-subtracted AOD of the stratosphere from the tropopause to 35  
 508 km altitude and averaged from -80 to 80° in latitude. a) AOD from main stratospheric  
 509 aerosol events caused by volcanic eruptions and wildfires. AOD<sub>50</sub> is shown (full grey  
 510 line) where correction due to lidar ratio deviating from 50 sr is undertaken (Pu11, Ra19  
 511 and Fi19&20). b) Yearly averages of data in a). Note that the horizontal tick marks  
 512 indicate start of a year in a) and the middle of a year in b). Also note that the averages of  
 513 years 2006 and 2023 span only half years due to the mid-year start (2006) and finish  
 514 (2023) of the CALIOP measurements.

515

516 The blue dots in Figure 8a over the stratospheric AOD were corrected for deviant lidar  
 517 ratios in 2011 (Puyehue-Cordón Caulle eruption) and 2019 – 2020 (Raikoke eruption and  
 518 Australian wildfires). The corresponding AOD using  $S_0 = 50$  sr is represented by a thin  
 519 gray line showing that the AOD was practically not affected by the correction in 2011  
 520 because that year was dominated by aerosol from another eruption (Nabro, Figure 3).

521 The AOD from the Raikoke (2019) eruption shifted down slightly by the correction, and  
522 that of the 2019 – 2020 Australian wildfires shifted upwards. Altogether the change in  
523 AOD from the corrections due to deviant lidar ratio were minor.

#### 524 **4.3 AOD of stratospheric aerosol events**

525 The AOD from aerosol events were approximately evenly distributed over the three  
526 latitude regions (SH, Tropics and NH) studied (Table 2). The altitude distribution showed  
527 most influence from volcanic eruptions and wildfires in the sBD (43%), followed by the  
528 dBD (31%), and the often overlooked LMS (Andersson et al., 2015) held 26% of the AOD  
529 from aerosol events in the period 2006 – 2023.

530 The average stratospheric AOD, with the contribution from background aerosol  
531 subtracted, from the tropopause to 35 km altitude in the latitude range -80 to 80° is  
532 shown in Figure 8a. The intense volcanism – sea interaction of the Hunga Ha’apai  
533 eruption in the beginning of 2022 (Martinsson et al., 2025) resulted in the highest and  
534 broadest AOD peak (Figure 8a). Other prominent events were the Australian wildfires at  
535 the end of 2019 and the beginning of 2020, the eruptions of Raikoke (2019), Sarychev  
536 (2009), Nabro (2011), Calbuco (2015) and Kasatochi (2008) affecting the stratospheric  
537 AOD together with several eruptions and wildfires having smaller contributions (Table  
538 1).

539 The average influence of volcanic eruptions and wildfires each year is shown in Figure  
540 8b. The most affected year was 2022 with an average AOD of 0.01 from aerosol events.  
541 That year is likely followed by 2023, for which we have no data from the second half of  
542 the year. Both these years were mainly affected by the 2022 Hunga Ha’apai eruption.  
543 Then follows 2020 (mainly the 2019-20 Australian wildfires with some contribution from  
544 the Raikoke eruption) with background-subtracted AOD of 0.006, 2009 (Sarychev) and  
545 2019 (Raikoke) both years with AOD of 0.005, whereas 2011 (mainly Nabro) reach AOD  
546 from aerosol events of almost 0.004. The average background-subtracted AOD from  
547 volcanic eruptions and wildfires from 2006 to 2023 is 0.0031. The background aerosol  
548 produces global average backscattering of  $0.00011 \text{ sr}^{-1}$ , which, with the commonly used  
549 assumption of a lidar ratio of 50 sr, corresponds to a stratospheric background AOD of  
550 0.0057.

551 The yearly average AOD from aerosol events ranges from 0.0002 (in 2013) to 0.010  
552 (2022) and the average over the 17 years studied is 0.0031. Making use of previous  
553 estimates of the relation between radiative forcing (F) and stratospheric AOD ( $F = -$   
554  $24 \times \text{AOD}$  in  $\text{W/m}^2$ ) (Schmidt et al., 2018), we estimate the radiative effect of the  
555 stratospheric aerosol events. This relation is based on volcanic sulfate aerosol, which is  
556 the dominant type of stratospheric aerosol event in the 17-year period studied. The  
557 relation is not designed to deal with absorbing wildfire aerosol, which could cause  
558 some uncertainty in the average radiative forcing of the period estimated here. The  
559 global stratospheric yearly average total effective radiative forcing due to volcanic  
560 eruptions and wildfires varies between  $-0.006$  and  $-0.24 \text{ W/m}^2$ , with the average  $-0.074$   
561  $\text{W/m}^2$  in the period 2006 to 2023. Assuming a lidar ratio of 50 sr, the stratospheric  
562 background aerosol effective radiative forcing becomes  $-0.14 \text{ W/m}^2$ .

#### 563 **4.4 The validity of AODs from CALIOP**

564 Stratospheric aerosol optical properties are often described using solar occultation  
565 data, especially from the 22 years of SAGE II measurements (Bauman et al., 2003;  
566 Thomason et al., 2018). Prior comparisons of CALIOP lidar-based results with solar  
567 occultation (SAGE III/ISS) show agreement within approximately 10% in the latitude  
568 range  $-30$  to  $30^\circ$  and increasing discrepancy at midlatitudes reaching above 50% at high  
569 latitudes for background aerosol in the altitude range 20 – 30 km (Kar et al., 2019), and  
570 discrepancies exceeding 50% is reported at altitudes below 17 km (Kovilakam et al.,  
571 2023). The main reason for these differences was attributed to the unknown lidar ratio  
572 of CALIOP (Kar et al., 2019; Kovilakam et al., 2023). Here we have estimated the CALIOP  
573 lidar ratio of the aerosol from several volcanic eruptions and wildfires (Figure 2), and in  
574 Figure 7d the latitude distribution of the estimates is shown. Using the standard lidar  
575 ratio of 50 sr cannot explain the latitude- and altitude-dependence in the lidar – solar  
576 occultation comparison obtained in Kar et al. (2019) and Kovilakam et al. (2023) for  
577 aerosol from volcanic eruptions and wildfires in the CALIOP era.

578 The latitude-dependent discrepancy at 532 nm wavelength between SAGE III/ISS and  
579 CALIOP at high altitudes in the period June 2017 to August 2018 above 20 km (, i.e.,  
580 essentially in the dBD) reported by Kar et al. (2019) concerns a period when the dBD  
581 was close to background (Figure 5). The method used here for estimating the lidar ratio

582 does not work for background conditions (Figure 1). Using 50 sr for background aerosol  
583 results in the global average background AOD of 0.0057. SAGE II measurements during  
584 the volcanically quiescent period 1998 – 2000 resulted in AOD of 0.0040 (estimated  
585 from Solomon et al. (2011), their Figure 2), who integrated the stratospheric AOD from  
586 15 km altitude. When removing the stratospheric aerosol data below 15 km from the  
587 CALIOP measurements, the stratospheric background AOD is reduced by 31% to  
588 0.0039 using lidar ratio 50 sr. This is almost identical to the background AOD reported in  
589 Solomon et al. (2011), thus indicating that the stratospheric background aerosol on  
590 average has a lidar ratio close to 50 sr. Kar et al. (2019) found that aerosol  
591 backscattering during background conditions at altitudes above 20 km in the  
592 extratropics should be converted to AOD by a variable lidar ratio. Mid- and high-latitude  
593 air in this altitude range has a high stratospheric age (~5 years) (Ploeger et al., 2021),  
594 implying that particle settling has long time to affect the size distribution, and hence the  
595 optical properties of the aerosol. In Figure 6c we find most of the aerosol above 20 km  
596 altitude in the tropics, implying that the deviations at high latitudes according to Kar et  
597 al. (2019) have little impact on global AOD, and thus little impact on our comparison  
598 dealing with the entire stratosphere above 15 km altitude.

599 In a comparison by Kovilakam et al. (2023) between CALIOP and SAGE III/ISS during  
600 November 2017, 2 – 3 months after the Canada/USA fire (Table 1) large deviations were  
601 found at high latitudes and altitudes as in Kar et al. (2019), as described above. That  
602 comparison also found large differences in the densest part of the stratosphere at  
603 altitudes below 17 km, where clouds frequently interfere with limb-viewing  
604 measurements. In GloSSAC the more than 50% lower values of limb-viewing  
605 techniques (SAGE and OSIRIS) than CALIOP were implemented citing uncertainties in  
606 the lidar ratio to discard CALIOP results at low altitudes (Kovilakam et al., 2023).

607 The main advantages of solar occultation measurements are that extinction is  
608 measured and that several wavelengths are available. With known lidar ratio, lidar  
609 measurements with nadir view have some distinct advantages compared to solar  
610 occultation limb views. Firstly, lidars have several hundred kilometers shorter  
611 measurement path enabling measurements in dense aerosol layers (Martinsson et al.,  
612 2022, their Figure 7) providing viable, quantitative results when limb views fail.

613 Secondly, the lidar vertical resolution is superior and is not relying on assumptions on  
614 homogeneity of the aerosol layer measured, like solar occultation measurements do  
615 (Damadeo et al., 2013). Accurate altitude descriptions with high vertical resolution of  
616 stratospheric injections (Sandvik et al., 2021) is vital for the outcome of stratospheric  
617 aerosol modeling (Axebrink et al., 2025). With these clear advantages we argue that  
618 lidar measurements should be given a more prominent role in stratospheric aerosol  
619 climatologies presented to the modeling community than in the present version (2.2) of  
620 GloSSAC (Thomason et al., 2018, Kovilakam et al., 2020; Kovilakam et al., 2023).

621 Hopefully the lidar ratio of stratospheric aerosol can be further clarified when the  
622 aerosol load is close to background conditions by lidar systems measuring both  
623 backscattering and extinction. The ATLID aboard the EarthCARE satellite (Illingworth et  
624 al., 2015) that started to produce data in July 2024 and the NASA and Italian Space  
625 Agency collaboration on the 3 wavelength lidar CALIGOLA planned for launch in the  
626 early 2030s (Behrenfeld et al., 2023) are future means to further clarify extinction  
627 obtained from lidars, and to optimally combine solar occultation and lidar  
628 measurements for future long-term records on the optical properties of the  
629 stratospheric aerosol with high and unambiguous vertical resolution.

## 630 **5. Conclusions**

631 The entire backscattering record at 532 nm wavelength of the satellite-based lidar  
632 system CALIOP spanning years 2006 to 2023 was investigated in this study. During this  
633 period injections of aerosol and precursor gases into the stratosphere of 15 volcanic  
634 eruptions and 5 wildfires were identified. The effective lidar ratios of 12 volcanic  
635 eruptions and wildfires were investigated to convert the measured backscattering to  
636 extinction. The measurements were evaluated and corrected for attenuation using the  
637 lidar ratio  $S_0 = 50$  sr. The aerosol events having a lidar ratio deviating by more than 5%  
638 from  $S_0$  were corrected after the general evaluation.

639 Background conditions are more probable in sublayers than in the entire stratosphere.  
640 The stratosphere was subdivided into 9 layers spanned by altitude (lowermost  
641 stratosphere (LMS), shallow Brewer-Dobson branch (sBD), deep Brewer-Dobson branch

642 (dBD)) and latitude intervals (tropics and Southern and Northern extratropics). The  
643 backgrounds of layers were combined to obtain that of the entire stratosphere. The  
644 backscattering of background aerosol was converted to aerosol optical depth (AOD)  
645 using a lidar ratio of 50 sr. That AOD agrees well with measurements with solar  
646 occultation (SAGE II) during 1998 – 2000 in the volcanically quiescent period. The  
647 average backscattering of seven of the nine layers each contains 11 - 15% of the entire  
648 background aerosol. The tropical LMS has a small contribution due to very small  
649 volume compared to the other layers. The tropical sBD was also clearly lower (7%)  
650 because oxidation of carbonyl sulfide (OCS) occurs at higher altitudes in the upwards  
651 moving air in the tropical stratosphere. We find that 70% of the aerosol in the tropical  
652 dBD is formed above 19 km altitude during background conditions, due to formation  
653 from OCS. Poleward followed by downward transport of the dBD aerosol to the sBD and  
654 LMS results in high aerosol concentrations at mid and high latitudes, whereas the  
655 polewards transport of tropical sBD air causes a band of low concentrations close to  
656 the tropopause at lower latitudes than the dBD air. Considering the ongoing debate on  
657 the sources of stratospheric background aerosol, these highly resolved CALIOP data  
658 could be useful to constrain modeling efforts on the subject.

659 The background aerosol was subtracted from the measurements to obtain the influence  
660 from aerosol and trace gas injections into the stratosphere. The most important aerosol  
661 events in the 17-year period are the 2022 Hunga Ha'apai eruption and the Australian  
662 wildfires (2019-20) followed by the volcanic eruptions Raikoke (2019), Sarychev (2009)  
663 and Nabro (2011). With the background AOD (0.0057) subtracted, the yearly average  
664 AOD spans 0 to 0.010. Using a simplified relation the yearly average effective radiative  
665 forcing of the background-subtracted aerosol is estimated to be in the range -0.006  
666 (year 2013) to -0.24 W/m<sup>2</sup> (2022).

667 Limb-viewing solar occultation measurements have some distinctive advantages in that  
668 much of the early measurements in the satellite era were undertaken with that method.  
669 They also deliver direct measurements of extinction, and at several wavelengths. Here,  
670 we have estimated the effective lidar ratio of the CALIOP measurements to obtain  
671 extinction from backscattering measurements. Lidars operating in nadir view, like  
672 CALIOP, have several hundred kilometers (or a factor of more than 100) shorter

673 measurement path than limb-viewers, allowing measurements in dense aerosol layers  
674 where limb-viewers fail. Lidars have unambiguous and superior vertical resolution over  
675 other satellite instruments providing models with important input data of aerosol and  
676 trace gas injections into the stratosphere. Newer lidars that measure extinction are  
677 launched, under construction and planned. Now is the time to better sort out  
678 differences between lidars and solar occultation measurements, especially in the  
679 dense stratospheric air located below 17 km altitude in records over the optical  
680 properties of the stratospheric aerosol.

## 681 **References**

- 682 Andersson, S. M., Martinsson, B. G., Friberg, J., Brenninkmeijer, C. A. M., Rauthe-  
683 Schöch, A., Hermann, M., van Velthoven, P. F. J., and Zahn, A.: Composition and  
684 evolution of volcanic aerosol from eruptions of Kasatochi, Sarychev and  
685 Eyjafjallajökull in 2008–2010 based on CARIBIC observations, *Atmos. Chem.*  
686 *Phys.*, 13, 1781–1796, <https://doi.org/10.5194/acp-13-1781-2013>, 2013.
- 687 Andersson, S. M., Martinsson, B. G., Vernier, J.-P., Friberg, J., Brenninkmeijer, C. A. M.,  
688 Hermann, M., van Velthoven, P. F. J., and Zahn, A.: Significant radiative impact of  
689 volcanic aerosol in the lowermost stratosphere, *Nat. Commun.*, 6, 1–8,  
690 <https://doi.org/10.1038/ncomms8692>, 2015.
- 691 Appenzeller, C., Holton, J.R., and Rosenlov, K.H.: Seasonal variation of mass transport  
692 across the tropopause, *J. Geophys. Res.* 101, 15071-15078, 1996.
- 693 Austin, J., and Li, F.: On the relationship between the strength of the Brewer-Dobson  
694 circulation and the age of stratospheric air, *Geophys. Res. Lett.*, 33, L17807,  
695 [doi:10.1029/2006GL026867](https://doi.org/10.1029/2006GL026867), 2006.
- 696 Axebrink, E., Sporre, M.K., and Friberg, J.: Impact of SO<sub>2</sub> injection profiles on simulated  
697 volcanic forcing for the 2009 Sarychev eruptions– investigating the importance of  
698 using high-vertical-resolution methods when compiling SO<sub>2</sub> data, *Atmos. Chem.*  
699 *Phys.*, 25, 2047–2059, <https://doi.org/10.5194/acp-25-2047-2025>, 2025.
- 700 Bauman, J. J., Russell, P. B., Geller, M. A., and Hamill, P.: A stratospheric aerosol  
701 climatology from SAGE II and CLAES measurements: 2. Results and  
702 comparisons, 1984–1999, *J. Geophys. Res.*, 108, 4383,  
703 <https://doi.org/10.1029/2002JD002993>, 2003.
- 704 Behrenfeld, M.J., Lorenzoni, L., Hu, Y., Bissom, K.M., Hostetler, C.A., Di Girolamo, P.,  
705 Dionisi, D., Longo, F., and Zoffoli, S.: Satellite Lidar Measurements as a Critical  
706 New Global Ocean Climate Record, *Remote Sens.* 15, 5567. [https://doi.org/](https://doi.org/10.3390/rs15235567)  
707 [10.3390/rs15235567](https://doi.org/10.3390/rs15235567), 2023.

- 708 Brühl, C., Lelieveld, J., Crutzen, P.J., and Tost, H.: The role of carbonyl sulphide as a  
709 source of stratospheric sulphate aerosol and its impact on climate, *Atmos.*  
710 *Chem. Phys.*, 12, 1239–1253, [www.atmos-chem-phys.net/12/1239/2012/](http://www.atmos-chem-phys.net/12/1239/2012/)  
711 [doi:10.5194/acp-12-1239-2012](https://doi.org/10.5194/acp-12-1239-2012), 2012.
- 712 Butchart, N., The Brewer-Dobson circulation, *Rev. Geophys.*, 52, 157–184,  
713 [doi:10.1002/2013RG000448](https://doi.org/10.1002/2013RG000448), 2014.
- 714 Carn, S.A., Krueger, A.J., Krotkov, N.A., Yang, K., and Evans, K.: Tracking volcanic sulfur  
715 dioxide clouds for aviation hazard mitigation, *Nat Hazards*, 51, 325–343 DOI  
716 10.1007/s11069-008-9228-4, 2009.
- 717 Carn, S.A., and Prata, F.J., Satellite-based constraints on explosive SO<sub>2</sub> release from  
718 Soufrière Hills Volcano, Montserrat, *Geophys. Res. Lett.*, 37, 1-5, L00E22,  
719 [doi:10.1029/2010GL044971](https://doi.org/10.1029/2010GL044971), 2010.
- 720 Carn, S. A., Krotkov, N. A., Fisher, B. L., and Li, C.: Out of the blue: Volcanic SO<sub>2</sub>  
721 emissions during the 2021–2022 eruptions of Hunga Tonga– Hunga Ha’apai  
722 (Tonga), *Front. Earth Sci.*, 10, 976962,  
723 <https://doi.org/10.3389/feart.2022.976962>, 2022.
- 724 Chin, M., and Davies, D.D.: A reanalysis of carbonyl sulfide as a source of stratospheric  
725 background sulfur aerosol, *J. Geophys. Res.* 100, 8993-9005, 1995.
- 726 Clarisse, L., Hurtmans, D., Clerbaux, C., Hadji-Lazaro, J., Ngadi, Y., and Coheur, P.-F.:  
727 Retrieval of sulphur dioxide from the infrared atmospheric sounding  
728 interferometer (IASI), *Atmos. Meas. Tech.*, 5, 581–594,  
729 <https://doi.org/10.5194/amt-5-581-2012>, 2012.
- 730 Clarisse, L., Coheur, P.-F., Prata F., Hadji-Lazaro, J., Hurtmans, D., and Clerbaux, C.: A  
731 unified approach to infrared aerosol remote sensing and type specification,  
732 *Atmos.Chem.Phys.*,13,2195–2221, [www.atmos-chem-phys.net/13/2195/2013/](http://www.atmos-chem-phys.net/13/2195/2013/)  
733 [doi:10.5194/acp-13-2195-2013](https://doi.org/10.5194/acp-13-2195-2013), 2013.
- 734 Crutzen, P.J.: The possible importance of CSO for the sulfate layer of the stratosphere,  
735 *Geophys. Res. Lett.* 3, 73-76, 1976.
- 736 Cruz, M.G., Sullivan, A.L., Gould, J.S., Sims, N.C., Bannister, A.J., Hollis, J.J., and Hurley,  
737 R.J.: Anatomy of a catastrophic wildfire: The Black Saturday Kilmore East fire in  
738 Victoria, Australia, *Forest Ecol. Manag.* 284, 269-295, 2012.
- 739 Damadeo, R.P., Zawodny, J.M., Thomason, L.W., and Iyer, N.: SAGE version 7.0  
740 algorithm: application to SAGE II, *Atmos. Meas. Tech.*, 6, 3539–3561,  
741 [www.atmos-meas-tech.net/6/3539/2013/](http://www.atmos-meas-tech.net/6/3539/2013/), 2013.
- 742 Friberg, J., Martinsson, B. G., Andersson, S. M., Brenninkmeijer, C. A. M., Hermann, M.,  
743 Van Velthoven, P. F. J., and Zahn, A.: Sources of increase in lowermost  
744 stratospheric sulphurous and carbonaceous aerosol background concentrations

745 during 1999–2008 derived from CARIBIC flights, *Tellus B*, 66, 23428,  
746 <https://doi.org/10.3402/tellusb.v66.23428>, 2014.

747 Friberg, J., Martinsson, B. G., Andersson, S. M., and Sandvik, O. S.: Volcanic impact on  
748 the climate– the stratospheric aerosol load in the period 2006–2015, *Atmos.*  
749 *Chem. Phys.*, 18, 11149–11169, <https://doi.org/10.5194/acp-18-11149-2018>,  
750 2018.

751 Friberg, J., Martinsson, B. G., and Sporre, M. K.: Short- and long-term stratospheric  
752 impact of smoke from the 2019–2020 Australian wildfires, *Atmos. Chem. Phys.*,  
753 23, 12557–12570, <https://doi.org/10.5194/acp-23-12557-2023>, 2023.

754 Fromm, M., Lindsey, D. T., Servranckx, R., Yue, G., Trickl, T., Sica, R., Doucet, P., and  
755 Godin-Beekmann, S.: The untold story of pyrocumulonimbus, *B. Am. Meteorol.*  
756 *Soc.*, 91, 1193–1209, 2010.

757 Fromm, M., Kablick III, G. P., Peterson, D. A., Kahn, R. A., Flower, V. J. B., and Seftor, C. J.:  
758 Quantifying the source term and uniqueness of the August 12, 2017 Pacific  
759 Northwest pyroCb event, *J. Geophys. Res.*, 126, e2021JD034928,  
760 <https://doi.org/10.1029/2021JD034928>, 2021.

761 Garofalo, L. A., Levin, E. J. T., Campos, T., Kreidenweis, S. N., and Farmer, D. K.:  
762 Emission and evolution of submicron organic aerosol in smoke from wild fires in  
763 the western United States, *ACS Space Chem.*, 3, 1237–1247, 2019.

764 Gelaro, R., McCarty, W., Suarez, M. J., Todling, R., Moloud, A., Takacs, L., Randles, C. A.,  
765 Darmenov, A., Bosilovich, M. G., Reichle, R., Wargan, K., Coy, L., Cullather, R.,  
766 Draper, C., Akella, S., Buchard, V., Conaty, A., da Silva, A. M., Gu, W., Kim, G.-K.,  
767 Koster, R., Lucchesi, R., Merkova, D., Nielsen, J. E., Partyka, G., Pawson, S.,  
768 Putman, W., Rienecker, M., Schubert, S. D., Seinkiewicz, M., and Zhao, B.: The  
769 Modern-Era Retrospective Analysis for Research and Applications, Version 2  
770 (MERRA-2), *J. Clim.* 30, 5419–5454, 2017.

771 Haywood, J.M., Jones, A., Clarisse, L., Bourassa, A., Barnes, J., Telford, P., Bellouin, N.,  
772 Boucher, O., Agnew, P., Clerbaux, C., Coheur, P., Degenstein, D., and Braesicke,  
773 P.: Observations of the eruption of the Sarychev volcano and simulations using  
774 the HadGEM2 climate model, *J. Geophys. Res.*, 115, D21212,  
775 [doi:10.1029/2010JD014447](https://doi.org/10.1029/2010JD014447), 2010.

776 Illingworth, A. J., Barker, H. W., Beljaars, A., Ceccaldi, M., Chepfer, H., Clerbaux, N.,  
777 Cole, J., Delanoë, J., Domenech, C., Donovan, D. P., Fukuda, S., Hidakata, M.,  
778 Hogan, R. J., Huenerbein, A., Kollias, P., Kubota, T., Nakajima, T., Nakajima, T. Y.,  
779 Nishizawa, T., Ohno, Y., Okamoto, H., Oki, R., Sato, K., Satoh, M., Shephard, M.  
780 W., Velázquez-Blázquez, A., Wandinger, U., Wehr, T., and van Zadelhoff, G.-J.: The  
781 Earth CARE Satellite: The Next Step Forward in Global Measurements of Clouds,  
782 Aerosols, Precipitation, and Radiation, *B. Am. Meteorol. Soc.*, 96, 1311–1332,  
783 <https://doi.org/10.1175/BAMS-D-12-00227.1>, 2015.

- 784 Junge, C.E., Chagnon, C.W., and Manson, J.E.: A World-wide Stratospheric Aerosol  
785 Layer, *Science*, 133, 1478-1479, 1961.
- 786 Kablick, G. P., Allen, D. R., Fromm, M. D., and Nedoluha, G. E.: Australian PyroCb Smoke  
787 Generates Synoptic-Scale Stratospheric Anticyclones, *Geophys. Res. Lett.*, 47,  
788 e2020GL08810, <https://doi.org/10.1029/2020GL088101>, 2020.
- 789 Kar, J., Lee, K.-P., Vaughan, M. A., Tackett, J. L., Trepte, C. R., Winker, D. M., Lucker, P. L.,  
790 and Getzewich, B. J.: CALIPSO level 3 stratospheric aerosol profile product:  
791 version 1.00 algorithm description and initial assessment, *Atmos. Meas. Tech.*,  
792 12, 6173–6191, <https://doi.org/10.5194/amt-12-6173-2019>, 2019.
- 793 Kloss, C., Berthet, G., Sellitto, P., Ploeger, F., Taha, G., Tidiga, M., Eremenko, M.,  
794 Bossolasco, A., Jégou, F., Renard, J.-B., and Legras, B.: Stratospheric aerosol  
795 layer perturbation caused by the 2019 Raikoke and Ulawun eruptions and their  
796 radiative forcing, *Atmos. Chem. Phys.*, 21, 535–560, <https://doi.org/10.5194/acp-21-535-2021>, 2021.
- 798 Kovilakam, M., Thomason, L.W., Ernest, N., Rieger, L.A., Bourassa, A.E., and Millán, L.:  
799 The Global Space-based Stratospheric Aerosol Climatology (version 2.0): 1979–  
800 2018, *Earth Syst. Sci. Data*, 12, 2607–2634, <https://doi.org/10.5194/essd-12-2607-2020>, 2020.
- 802 Kovilakam, M., Thomason, L.W., and Knepp, T.: SAGEIII/ISS aerosol/cloud categorization  
803 and its impact on GloSSAC, *Atmos. Meas. Tech.*, 16, 2709–2731,  
804 <https://doi.org/10.5194/amt-16-2709-2023>, 2023.
- 805 Kremser, S., Thomason, L. W., von Hobe, M., Hermann, M., Desher, T., Timmreck, C.,  
806 Toohey, M., Stenke, A., Schwarz, J. P., Weigel, R., Fueglistaler, S., Prata, F. J.,  
807 Vernier, J. P., Schlager, H., Barnes, J. E., Antuña-Marrero, J. C., Fairlie, D., Palm,  
808 M., Mahieu, E., Notholt, J., Rex, M., Bingen, C., Vanhellemont, F., Bourassa, A.,  
809 Plane, J. M. C., Klocke, D., Carn, S. A., Clarisse, L., Trickl, T., Neely, R., James, A.  
810 D., Rieger, L., Wilson, J. C., and Meland, B.: Stratospheric aerosol– Observations,  
811 processes, and impact on climate, *Rev. Geophys.*, 54, 278–335,  
812 <https://doi.org/10.1002/2015RG000511>, 2016.
- 813 Li, C., Krotkov, N.A., Carn, S., Zhang, Y., Spurr, R.D.J., and Joiner, J.: New-generation  
814 NASA Aura Ozone Monitoring Instrument (OMI) volcanic SO<sub>2</sub> dataset: algorithm  
815 description, initial results, and continuation with the Suomi-NPP Ozone Mapping  
816 and Profiler Suite (OMPS), *Atmos. Meas. Tech.*, 10, 445–458, [www.atmos-meas-  
817 tech.net/10/445/2017/](http://www.atmos-meas-tech.net/10/445/2017/), doi:10.5194/amt-10-445-2017, 2017.
- 818 Lin, P., and Fu, Q., Changes in various branches of the Brewer–Dobson circulation from  
819 an ensemble of chemistry climate models, *J. Geophys. Res.*, 118, 73–84,  
820 doi:10.1029/2012JD018813, 2013.
- 821 Malinina, E., Rozanov, A., Niemayer, U., Wallis, S., Arosio, C., Wrana, F., Timmreck, C.,  
822 von Savigny, C., and Burrows, J.P.: Changes in stratospheric aerosol extinction

823 coefficient after the 2018 Ambae eruption as seen by OMPS-LP and MAECHAM5-  
824 HAM, *Atmos. Chem. Phys.*, 21, 14871–14891, [https://doi.org/10.5194/acp-21-](https://doi.org/10.5194/acp-21-14871-2021)  
825 14871-2021, 2021.

826 Martinsson, B. G., Nguyen, H. N., Brenninkmeijer, C. A. M., Zahn, A., Heintzenberg, J.,  
827 Hermann, M., and Velthoven, P. F. J. v.: Characteristics and origin of lowermost  
828 stratospheric aerosol at northern midlatitudes under volcanically quiescent  
829 conditions based on CARIBIC observations, *J. Geophys. Res.*, 110, D12201,  
830 doi:10.1029/2004JD005644, 2005.

831 Martinsson, B. G., Brenninkmeijer, C. A. M., Cam, S. A., Hermann, M., Heue, K.P., van  
832 Velthoven, P. F. J., and Zahn, A.: Influence of the 2008 Kasatochi volcanic  
833 eruption on sulfurous and carbonaceous aerosol constituents in the lower  
834 stratosphere, *Geophys. Res. Lett.*, 36, 1–5,  
835 <https://doi.org/10.1029/2009GL038735>, 2009.

836 Martinsson, B. G., Friberg, J., Sandvik, O. S., Hermann, M., van Velthoven, P. F. J., and  
837 Zahn, A.: Formation and composition of the UTLS aerosol, *npj Climate and*  
838 *Atmospheric Science*, 2, 1–6, <https://doi.org/10.1038/s41612-019-0097-1>, 2019.

839 Martinsson, B. G., Friberg, J., Sandvik, O. S., and Sporre, M. K.: Five-satellite-sensor  
840 study of the rapid decline of wildfire smoke in the stratosphere, *Atmos. Chem.*  
841 *Phys.*, 22, 3967–3984, <https://doi.org/10.5194/acp-22-3967-2022>, 2022.

842 Martinsson, B. G., Friberg, J., and Sporre, M. K.: Stratospheric aerosol formed by intense  
843 volcanism–sea interaction during the 2022 Hunga Ha’apai eruption, *Atmos.*  
844 *Chem. Phys.*, 25, 10677–10690, <https://doi.org/10.5194/acp-25-10677-2025>,  
845 2025.

846 Mastin, L. G., Van Eaton, A. R., and Cronin, S. J.: Did steam boost the height and growth  
847 rate of the giant Hunga eruption plume?, *B. Volcanol.*, 86, 64,  
848 <https://doi.org/10.1007/s00445-024-01749-1>, 2024.

849 McCarthy, G.J., Plucinski, M.P., and Gould, J.S.: Analysis of the resourcing and  
850 containment of multiple remote fires: The Great Divide Complex of fires, Victoria,  
851 December 2006, *Australian Forestry*, 75, 54-63, DOI:  
852 10.1080/00049158.2012.10676385, 2012.

853 Mote, P.W., Dunkerton, T.J., McIntyre, M.E., Ray, E.A., Haynes, P.H., and Russell III, J.M.:  
854 Vertical velocity, vertical diffusion, and dilution by midlatitude air in the tropical  
855 lower stratosphere, *J. Geophys. Res.* 103, 8651-8666, 1998.

856 Murphy, D. M., Cziczo, D. J., Hudson, P. K., and Thomson, D. S.: Carbonaceous material  
857 in aerosol particles in the lower stratosphere and tropopause region, *J. Geophys.*  
858 *Res.*, 112, D04203, <https://doi.org/10.1029/2006JD007297>, 2007.

859 NASA/LARC/SD/ASDC: Science CALIPSO Lidar Level 1B profile data, V4-51, NASA  
860 Langley Atmospheric Data Center DAAC,  
861 [https://doi.org/10.5067/CALIOP/CALIPSO/CAL\\_LID\\_L1 Standard-V4-51](https://doi.org/10.5067/CALIOP/CALIPSO/CAL_LID_L1 Standard-V4-51), 2024.

- 862 Nicknish, P.A., Stone, K., Solomon, S., and Carn, S.A.: Quantifying the decay timescale  
863 of volcanic sulfur dioxide in the stratosphere, *Atmos. Chem. Phys.*, 25, 11535–  
864 11555, <https://doi.org/10.5194/acp-25-11535-2025>, 2025.
- 865 Ohneiser, K., Ansmann, A., Baars, H., Seifert, P., Barja, B., Jimenez, C., Radenz, M.,  
866 Tiesseire, A., Floutsi, A., Haarig, M., Foth, A., Chudnovsky, A., Engelmann, R.,  
867 Zamorano, F., Bühl, J., and Wandinger, U.: Smoke of extreme Australian bushfires  
868 observed in the stratosphere over Punta Arenas, Chile, in January 2020: optical  
869 thickness, lidar ratios, and depolarization ratios at 355 and 532nm, *Atmos.*  
870 *Chem. Phys.*, 20, 8003–8015, <https://doi.org/10.5194/acp-20-8003-2020>, 2020.
- 871 Pardini, F., Burton, M., Arzilli, F., La Spina, G., and Polacci, M.: SO<sub>2</sub> emissions, plume  
872 heights and magmatic processes inferred from satellite data: The 2015 Calbuco  
873 eruptions, *J. Volcanol. Geotherm. Res.* 361, 12-24, 2018.
- 874 Peterson, D. A., Fromm, M. D., McRae, R. H. D., Campbell, J. R., Hyer, E. J., Taha, G.,  
875 Camacho, C. P., Kablick, G. P., Schmidt, C. C., and DeLand, M. T.: Australia's  
876 Black Summer pyrocumulonimbus super outbreak reveals potential for  
877 increasingly extreme stratospheric smoke events, *Npj Clim. Atmos. Sci.*, 4, 38  
878 <https://doi.org/10.1038/s41612-021-00192-9>, 2021.
- 879 Peterson, D. A., Berman, M. T., Fromm, M. D., Servranckx, R., Julstrom, W. J., Hyer, E. J.,  
880 Campbell, J. R., McHardy, T. M., and Lambert, A.: Worldwide inventory reveals  
881 the frequency and variability of pyrocumulonimbus and stratospheric smoke  
882 plumes during 2013–2023, *Npj Clim. Atmos. Sci.*, 8, 325,  
883 <https://doi.org/10.1038/s41612-025-01188-5>, 2025.
- 884 Ploeger, F., Diallo, M., Charlesworth, E., Konopka, P., Legras, B., Laube, J.C., Gross, J.-U.,  
885 Günther, G., Engel, A., and Riese, M.: The stratospheric Brewer–Dobson  
886 circulation inferred from age of air in the ERA5 reanalysis, *Atmos. Chem. Phys.*,  
887 21, 8393–8412, <https://doi.org/10.5194/acp-21-8393-2021>, 2021.
- 888 Prata, A. T., Young, S. A., Siems, S. T., and Manton, M. J.: Lidar ratios of stratospheric  
889 volcanic ash and sulfate aerosols retrieved from CALIOP measurements, *Atmos.*  
890 *Chem. Phys.*, 17, 8599–8618, <https://doi.org/10.5194/acp-17-8599-2017>, 2017.
- 891 Rieger, L.A., Bourassa, A.E., and Degenstein, D.A.: Merging the OSIRIS and SAGE II  
892 stratospheric aerosol records, *J. Geophys. Res. Atmos.*, 120, 8890–8904,  
893 doi:10.1002/2015JD023133, 2015.
- 894 Sandvik, O. S., Friberg, J., Sporre, M. K., and Martinsson, B. G.: Methodology to obtain  
895 highly resolved SO<sub>2</sub> vertical profiles for representation of volcanic emissions in  
896 climate models, *Atmos. Meas. Tech.*, 14, 7153–7165,  
897 <https://doi.org/10.5194/amt-14-7153-2021>, 2021.
- 898 Sato, M., Hansen, J.E., McCormick, M.P., and Pollack J.B.: Stratospheric aerosol optical  
899 depths, 1850-1990, *J. Geophys. Res.* 98, 22987-22994, 1993.

900 Schmidt, A., Mills, M. J., Ghan, S., Gregory, J. M., Allan, R. P., Andrews, T., Bardeen, C. G.,  
901 Conley, A., Forster, P. M., Gettelman, A., Portmann, R. W., Solomon, S., and Toon,  
902 O. B.: Volcanic radiative forcing from 1979 to 2015, *J. Geophys. Res.-Atmos.*, 123,  
903 12491–12508, <https://doi.org/10.1029/2018JD028776>, 2018.

904 Seabrook, S., Mackay, K., Watson, S. J., Clare, M. A., Hunt, J. E., Yeo, I. A., Lane, E. M.,  
905 Clark, M. R., Wysoczanski, R., Rowden, A.A., Kula, T., Hoffmann, L.J., Armstrong,  
906 E., and Williams, M. J. M.: Volcaniclastic density currents explain widespread  
907 and diverse seafloor impacts of the 2022 Hunga Volcano eruption, *Nat.*  
908 *Commun.*, 14, 7881, <https://doi.org/10.1038/s41467-023-43607-2>, 2023.

909 Sheng, J.-X., Weisenstein, D.K., Luo, B.-P., Rozanov, E., Stenke, A., Anet, J., Bingemer, H.,  
910 and Peter, T.: Global atmospheric sulfur budget under volcanically quiescent  
911 conditions: Aerosol-chemistry-climate model predictions and validation, *J.*  
912 *Geophys. Res. Atmos.*, 120, 256–276, doi:10.1002/2014JD021985, 2015.

913 Solomon, S., Daniel, J. S., Neely, R. R., Vernier, J.-P., Dutton, E. G., and Thomason, L. W.:  
914 The persistently variable “background” stratospheric aerosol layer and global  
915 climate change, *Science*, 333, 866–870, 2011.

916 Surano, Jousset, P., Pallister, J., Boichu, M., Boungiorno, M.F., Budisantoso, A., Costa, F.,  
917 Andreastuti, S., Prata, F., Schneider, D., Clarisse, L., Humaida, H., Sumarti, S.,  
918 Bignami, C., Griswold, J., Carn, S., Oppenheimer C., and Lavigne F.: The 2010  
919 explosive eruption of Java's Merapi volcano—A ‘100-year’ event, *J. Volcanol.*  
920 *Geotherm. Res.* 241-242, 121-135, 2012.

921 Taylor, I. A., Grainger, R. G., Prata, A. T., Proud, S. R., Mather, T. A., and Pyle, D. M.: A  
922 satellite chronology of plumes from the April 2021 eruption of La Soufrière, St  
923 Vincent, *Atmos. Chem. Phys.*, 23, 15209–15234, [https://doi.org/10.5194/acp-23-](https://doi.org/10.5194/acp-23-15209-2023)  
924 [15209-2023](https://doi.org/10.5194/acp-23-15209-2023), 2023.

925 Thomas, H.E., Watson, I.M., Carn, S.A., Prata, A.J., and Realmuta, V.J.: A comparison of  
926 AIRS, MODIS and OMI sulphur dioxide retrievals in volcanic clouds, *Geomatics,*  
927 *Natural Hazards and Risk*, 2, 217-232, 2011.

928 Thomason, L.W., Ernest, N., Millán, L., Rieger, L., Bourassa, A., Vernier, J.-P., Manney, G.,  
929 Luo, B., Arfeuille, F., and Peter, T.: A global space-based stratospheric aerosol  
930 climatology: 1979-2016, *Earth Syst. Sci. Data*, 10, 469–492,  
931 <https://doi.org/10.5194/essd-10-469-2018>, 2018.

932 Vernier, J.-P., Pommereau, J.P., Garnier, A., Pelon, J., Larsen, N., Nielsen, J.,  
933 Christiansen, T., Cairo, F., Thomason, L.W., Leblanc, T., and McDermid, I.S.:  
934 Tropical stratospheric aerosol layer from CALIPSO lidar observations, *J.*  
935 *Geophys. Res.*, 114, D00H10, doi:10.1029/2009JD011946, 2009.

936 Vernier, J.-P., Farlie, T.D., Murray, J.J., Tupper, A., Trepte, C., Winker, D., Pelon, J., Garnier,  
937 A., Jumelet, J., Pavolonis, M., Omar, A.H., and Powell, K.A.: An Advanced System

938 to Monitor the 3D Structure of Diffuse Volcanic Ash Clouds *J. Appl. Meteorol.*  
939 *Clim.* 10, 2125-2138, 2013.

940 Vernier, J.-P., Farlie, T.D., Natarajan, M., Wiengold, F.G., Bian, J., Martinsson, B.G.,  
941 Crumeyrolle, S., Thomason, L.W., and Bedka, K.M.: Increase in upper  
942 tropospheric and lower stratospheric aerosol levels and its potential connection  
943 with Asian pollution, *J. Geophys. Res.*, 120, doi:10.1002/2014JD022372, 2015.

944 Weisenstein, D.K., Yue, G.K., Ko, M.K.W., Sze, N.-D., Rodriguez, J.M., and Scott, C.J.: A  
945 two-dimensional model of sulfur species and aerosol, *J. Geophys. Res.* 102,  
946 13019-13035, 1997.

947 Winker, D. M., Hunt, W. H., and McGill, M. J.: Initial performance assessment of CALIOP,  
948 *Geophys. Res. Lett.*, 34, 1–5, <https://doi.org/10.1029/2007GL030135>, 2007.

949 Winker, D. M., Pelon, J., Coakley, J. A., Ackerman, S. A., Charlson, R. J., Colarco, P. R.,  
950 Flamant, P., Fu, Q., Hoff, R. M., Kittaka, C., Kubar, T. L., Le Treut, H., McCormick,  
951 M. P., Mégie, G., Poole, L., Powell, K., Trepte, K., Vaughan, M. A., and Wielicki, B.  
952 A.: The CALIPSO mission—A global 3D view of aerosols and clouds, *B. Am.*  
953 *Meteorol. Soc.*, 91, 1211–1229, <https://doi.org/10.1175/2010BAMS3009.1>, 2010.

954 *Data availability.* The data used are publicly available: CALIOP V4.51 lidar data  
955 (<https://search.earthdata.nasa.gov/search?fp=CALIPSO>).

956 *Author contributions.* BGM planned the study, undertook most of the data analysis and  
957 wrote the paper. JF participated in the planning of the study, undertook part of the data  
958 analysis and MKS contributed. JF and MKS undertook data extraction and handling for  
959 the data analysis. All authors participated in discussions and commented on the  
960 manuscript.

961 *Disclaimer.* The contact author and the co-authors declare that they have no competing  
962 interests.

963 *Acknowledgements.* Aerosol products from the CALIOP sensor were produced by NASA  
964 Langley Research Center.

965 *Financial support.* The Swedish National Space Agency, contracts 2025-00200 and  
966 2022-00157, Johan Friberg. The Crafoord Foundation, contract 20240901, Johan Friberg.  
967 Formas, contract 2020-00997, Moa Sporre. The Swedish Research Council 2022-02836,  
968 Moa Sporre.